2020-01-01

SYNThesis and Characterization of Novel Lithium Gallium Phosphate (LiGaP2O7) for Extreme Environment Applications

Mohan Raj Rajkumar
University of Texas at El Paso

SYNTHESIS AND CHARACTERIZATION OF NOVEL LITHIUM GALLIUM PHOSPHATE ($LiGaP_2O_7$) FOR EXTREME ENVIRONMENT APPLICATIONS

MOHAN RAJ RAJKUMAR

Master's Program in Mechanical Engineering

APPROVED:

Chintalapalle Ramana, Ph.D., Chair

Alejandra G. Castellanos, Ph.D.

David A. Roberson, Ph.D.

Chunqiang Li, Ph.D.

Stephen L. Crites, Jr., Ph.D.
Dean of the Graduate School

Dedication

I dedicate this to my family and friends. My dad, who has always trusted me to find my way in the world, my mom, who has never stopped worrying about me and finally, my sister, who has always supported and advised me in all my ventures. My friends, from the people who were right here to the once across the world, thank you for entertaining all various moods over the years.

SYNTHESIS AND CHARACTERIZATION OF NOVEL LITHIUM GALLIUM PHOSPHATE ($LiGaP_2O_7$) FOR EXTREME ENVIRONMENT APPLICATION

by

MOHAN RAJ RAJKUMAR, B.E.

THESIS

Presented to the Faculty of the Graduate School of

The University of Texas at El Paso

in Partial Fulfillment

of the Requirements

for the Degree of

MASTER OF SCIENCE

Department of Mechanical Engineering

THE UNIVERSITY OF TEXAS AT EL PASO

August 2020

Acknowledgments

I would like to thank everyone that contributed, supported, and enabled me to complete my thesis. To start, I would like to express my heartfelt gratitude to my research advisor, Dr. Chintalapalle Ramana, without whom I would not have had this great opportunity. The time I spent performing research under his guidance was a life-changing experience. The members of Center for Advanced Materials Research (CMR), my research group, were not only a group of people whom I could learn more from and talk science with but were also an unshakable support system who were always there when I needed it and for helping me in various experiments. My heartfelt thank you for everything they have done for me. I also would like to sincerely acknowledge the funding agencies supporting CMR and enabling students to excel in research and educational activities. And finally, I would like to thank the other professors who have taught me through these two years, the mechanical department, and the university itself for this beautiful learning environment.

Abstract

In this work, we report on the synthesis, characterization, and performance of $LiGaP_2O_7$ (LGP), a novel material and new to the scientific & engineering community. $LiGaP_2O_7$ materials were was synthesized using the conventional high-temperature, solid-state ceramic reaction. Calcination was done in three steps at the temperatures of 300 °C, 500 °C, and 650 °C for 8 h each to ensure a single phase. Utilizing this, different green pellets were sintered at 800 °C for varying times of 3 h, 6 h, 12 h, and 24 h. The structure, phase, and morphology were analyzed using X-ray diffraction (XRD) and scanning electron microscopy (SEM). Furthermore, structural refinement was done utilizing the Rietveld method. The crystallite size decreased, grain size increased, and the volume of the unit cell decreased due to increasing sintering time. The dielectric properties of LGP samples were measured as a function of temperature and frequency. The modified Debye's equation and Cole-Cole plot were used, which indicated multiple ions were responsible for dielectric relaxation. The dielectric constant decreases as a function of increasing frequency, indicating a lack of polarization sources contribution and increases as a function of increasing temperature, indicating thermal activation of charge carriers. The study of the type of conduction mechanism using AC conductivity indicated at hoping type conduction.

The LGP films were deposited by pulsed-laser deposition (PLD) using a target (sintered at 800 °C for 12 h). The substrate temperature (T_s) was varied from 25 to 700 °C to. The PLD LGP films were nanocrystalline at ≥500 °C. Spectroscopic ellipsometry analyses indicate a decrease in film thickness and refractive index with T_s. Moreover, the extinction coefficient suggested luminance at a specific frequency. Second-harmonic generation (SHG) measurements were made to measure the nonlinear optical properties. The results indicated the dependency of SHG signal on the structure and morphology of LGP films. The structure-property correlation is established.

Table of Contents

List of Tables

List of Figures

Chapter 1: Introduction

Phosphorus (P) is one of the most common elements in our environment and is essential to all life. Phosphate is an anion derived from phosphoric acid. Phosphate $[PO_4]^{3-}$, pyrophosphate, or diphosphates $[P_2O_7]^{4-}$, polyphosphate $[HPO_3]_n$, metaphosphate $[PO^n{}_3]$ are just a few of its wide variations.

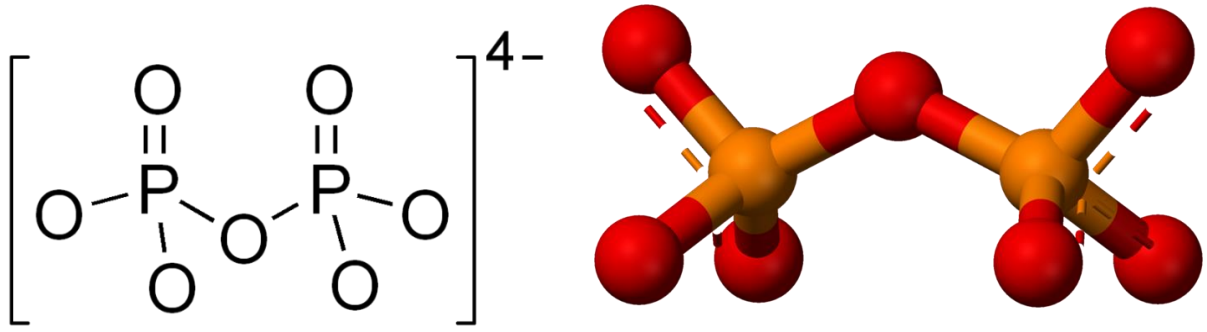

Figure 1.1: (Left) Structural formula of diphosphate (Kemikungen from Wikipedia). (Right) 3D diphosphate. Red balls represent oxygen, and orange-yellow represents phosphorus. (Benjah-bmm27 from Wikipedia)

From their discovery in the late 1800s, phosphate based materials continue to be extensively studied all over the world due to their fascinating physical properties and potential technological applications, some of which are luminescence, ionic conductors, ferroelectric, and solid-state laser materials [1–8]. Calcium phosphate bioceramics have good biocompatibility, osseointegration, and osteoconduction. Hence they are widely used in the field of bone regeneration, both in orthopedics and in dentistry [9]. Porous nanomaterials consisting of interconnected micropores, mesopores, and macropores are possible due to metals phosphates [10]. Research in cobalt phosphate and nickel phosphate have shown them to be suitable materials for high-performance supercapacitors [11]. Lead hydrogen phosphate, a type of hydrogen-bonded ferroelectric material, is a reference to understand photon ordering in hydrogen-bonded ferroelectric materials [12]. Research has shown positive results in glassy zirconium phosphates

as super protonic conductors [13], a variety of new copper phosphates materials as ionic or mixed conductors [14].

Pyrophosphate or diphosphates $[P_2O_7]^{4-}$ (a molecule containing two phosphorous atoms in a P-O-P arrangement) is one of the main interests of researchers worldwide. Due to the excellent optical properties of diphosphates, materials such as $NaScP_2O_7$ [15], $KErP_2O_7$ [16], KYP_2O_7 [17,18], $AgLaP_2O_7$ [19], and $SrMgP_2O_7$ doped with rare earth materials [20], $AgYP_2O_7$ [21] and MYP_2O_7 (M=Rb,Cs) [17] are just a few that have been extensively researched.

For use in an extreme environment, phosphates have been studied in-depth and have shown promising results. Most importantly, phosphate materials enable the operation and utilization under extreme environments of very high temperatures and deep ultraviolet (UV) conditions. For instance, $(ZrO)_2P_2O_7$ has stable existence to temperatures around 1600 °C and is characterized by a very low linear thermal expansion coefficient [22]. Similarly, for high-temperature sensors, gallium phosphate ($GaPO_4$) is a new promising piezoelectric crystal material. It has a crystal structure like quartz but a much higher thermal stability. It can be used in the temperature ranges up to 900 °C [23]. On the other hand, many of the diphosphate based solid state materials continue to the attractive choice for optical and electronic devices operating in the extreme regions of infrared (IR) and deep UV regions of the electromagnetic spectrum.

In the late 20th century, increasing demand for energy storage due to technological advancements led to a significant amount of research and development of lithium-based battery electrolytes and electrodes. Its high electrode potential with low atomic mass made it the ideal material. Furthermore, with the development of electric vehicles, Li-ion batteries possessed the power and energy densities necessary for its application [24]. One of the most promising

candidates for high-energy-density energy storage devices is lithium metal batteries. However, they are not practically used due to low cycling efficiency and severe safety concerns [25].

Nevertheless, given time for research and development, these shortcomings could be overcome. Moreover, with the energy demand not reducing soon, better and efficient materials are sought after with, one such focus being lithium phosphates.

The motivation to the present work, which is integrating the excellent properties of Li-based phosphates into a well-known wide band gap electronic material, is derived from the following considerations. For a long time, silicon-based power electronic devices have had a vast presence, but with a multitude of application requirements, but now they alone are hard to satisfy them all. Gallium oxide (Ga_2O_3), is a typical ultra-wide bandgap semiconductor and has shown promise where high-power and high-voltage devices are required [26]. Moreover, the most stable phase of gallium oxide is β-Ga_2O_3 [27]. Furthermore, it can be used for the application of solar-blind UV photodetectors [28,29], transparent field-effect transistor[30], and even Schottky barrier diode [31]. Therefore, the present work is an attempt to design and develop materials, where the advantages of widen band gap electronic material and excellent structural and optical properties of phosphates can be combined.

1.1 Motivation and Research Objectives

Based on our group's previous research on the Li-insertion/extraction processes in $LiFePO_4/FePO_4$, where the results invalidated the previous models used and suggested a new model [32], and the work on $LiFe_{1.5}P_2O_7$ centered around positive electrode application in Li-ion battery [33], lithium phosphates were shown to be a new promising avenue of research. This is owing to their electrical properties and potential in a battery application. $LiVP_2O_7$ [34], $LiFeP_2O_7$, and $LiScP_2O_7$ [35] were some of the lithium phosphates materials explored by other researchers

for a similar application. Moreover, in our research group's previous work, Ga based compounds [36] also showed excellent electric and optical properties, which could be tuned as required. This is the motivation of our present work on $LiGaP_2O_7$ (LGP).

LGP is a new material that has not yet been explored except for one work that reported on its potential as a UV nonlinear-optical crystal [37]. In fact, when our research group initiated the work few years ago, there were no reports in the literature. The purpose of the present work is to study its synthesis, structure, electrical and dielectric properties, conduction mechanism, thin film deposition, and optical properties. This is all in pursuit of optimizing the material with high structural quality and desired properties for enhanced performance in optical and electronic devices.

The specific objectives are as follows:

1) Ceramic synthesis.
2) Structural characterization focusing on the effect of sintering condition.
3) Evaluating dielectric properties and conduction mechanism.
4) Fabrication of LGP thin films by pulsed laser deposition.
5) Structural and morphological analysis of the thin film as a function of substrate temperature.
6) Exploring the optical properties of LGP thin film.

Chapter 2: Literature Review

Lithium diphosphate ceramics $LiMP_2O_7$ (M: transition metal) are extensively looked at for their potential in battery applications due to their physical properties. Some of these battery applications include medical devices, electric vehicles, laptops, and cellphones. One of the physical properties that is most important is the high mobility of lithium ions, which promotes the insertion/extraction reactions [32,36,38]. Materials having a P_2O_7 framework make excellent solid electrolytes and electrodes materials in rechargeable batteries [39,40] as they undergo frameworks where tunnels are accessible for mobile cations such as alkali (Na^+, Li^+) ions [40–42]. The appearance of the symmetric and antisymmetric P-O-P stretching vibration is specific to diphosphates and can be termed as its specific spectral fingerprints [43].In the past few years, the electrical properties of lithium diphosphates such as $LiFeP_2O_7$ and $LiCrP_2O_7$ have been reported [44,45]. Diphosphates such as $LiFeP_2O_7$ and $LiScP_2O_7$ show similar ionic conductivity as they are isostructural. Moreover, they show low lithium-ion conductivity despite having had a framework with sufficiently wide tunnels (bottlenecks of 3.96 Å) for lithium-ion transport along the c-axis [35].

Lithium-gallium based pyrophosphate (referred to LGP throughout this thesis) is a noncentrosymmetric pyrophosphate which crystallizes in the monoclinic space group $P2_1$. Noncentrosymmetric is an important feature of piezoelectric material [46]. The lattice parameters of LGP are a = 4.7593(10) Å, b = 7.9586(16) Å, c = 6.8940(14) Å, β = 109.06(3) ° and Z = 2 with a bandgap of 4.56eV.It is an isomorphic compound of $LiFeP_2O_7$ (bandgap of 2.58 eV) and $LiCrP_2O_7$ (bandgap of 1.6 eV). LGP has no d-d electronic transition due to which it exhibits a wide

bandgap of 4.56 eV when compared to $LiMP_2O_7$ [37]. For comparison, monoclinic β-Ga_2O_3 has an ultrawide bandgap of ~ 4.8 eV [27].

The asymmetric LGP has seven unique O atoms, two unique P atoms, one unique Ga atom, and one unique Li atom. A [P_2O_7] dimer is formed by sharing the corner oxygen of two basic [PO_4] blocks, as shown in Figure 2.1. A [GaO_6] octahedra are formed from the Ga atom and six oxygen atoms where three Ga-O bonds are longer than the others and are linked to the [P_2O_7] dimer via corner-sharing. The Li atom is coordinated to four O atoms to constitute a [LiO_4] tetrahedron. However, the O–Li–O intersection angles are far from that of the regular [LiO_4] tetrahedron. Moreover, all the bonded O atoms are on the same side of the Li atom and exhibit a typical "see-saw"-type configuration, as shown in Figure 2.2. Hence, the LiO_4 tetrahedron is seriously distorted [37].

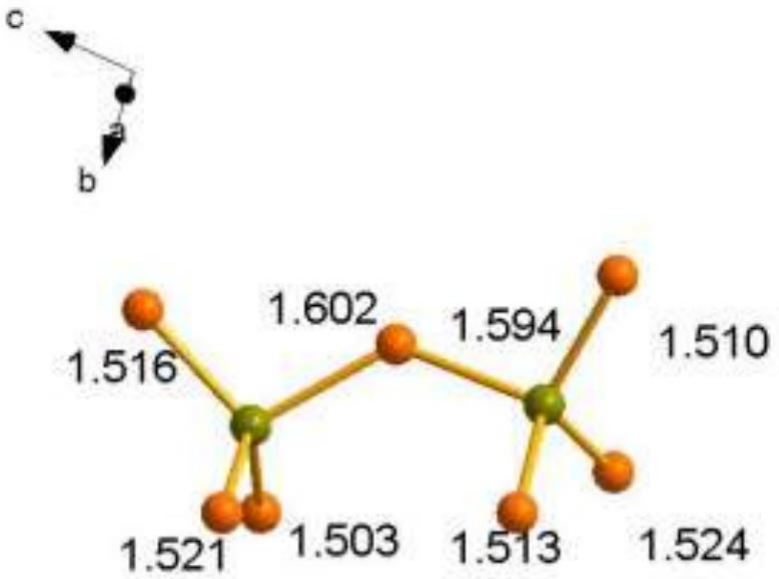

Figure 2.1: [P_2O_7] dimer in LGP where green is phosphorus and orange is oxygen (Supporting information from [37])

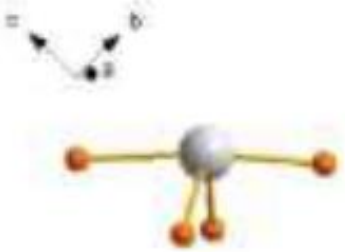

Figure 2.2: [LiO_4] tetrahedron in LGP where grey is lithium and orange is oxygen (Supporting information from [37])

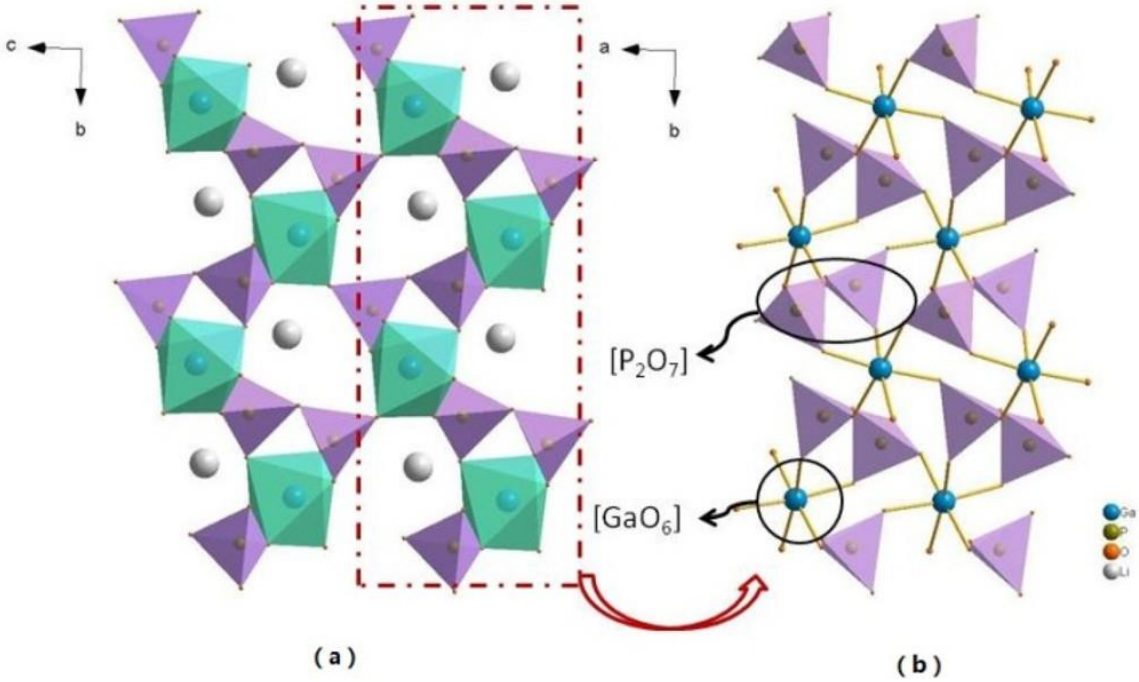

Figure 2.3: Blue represents Ga, green represents P, orange represents O and grey represents Li. (a) Projection of $LiGaP_2O_7$ in the [100] direction. (Lilac tetrahedra represent the PO_4 and light-green octahedra represent the GaO_6 groups.) (b) 2D zigzag [GaP_2O_{11}] layers in the ab plane. (From [37])

Chapter 3: Experimental Methods

3.1 Solid-State Synthesis Reaction

A solid-state synthesis reaction utilizes solid reagents to obtain polycrystalline materials.[47] LGP has been synthesized using a conventional solid-state reaction based on stoichiometric calculations. The solid-state reaction can be written as follows:

$$Li_2CO_3 + Ga_2O_3 + 4NH_4H_2PO_4 \longrightarrow 2LiGaP_2O_7 + 4NH_3\,(g) + 6H_2O\,(g) + CO_2\,(g) \quad (1)$$

The precursors used, Li_2CO_3 (99.99%), $NH_4H_2PO_4$ (99.99%), and Ga_2O_3 (≥99.99%), were obtained from Sigma-Aldrich. An agate mortar was used to mix and pulverize the precursors with the help of acetone as a wetting medium for 2 h to ensure homogeneity. The mixture was transferred into crucibles for calcination in a muffle furnace. For the removal of volatile compounds (i.e., of NH_3, H_2O, and CO_2), calcination was done in three steps at the temperatures of 300 °C, 500 °C and 650 °C for 8 h each. The sample was ground in an agate mortar in-between each step to ensure uniformity and assist the process.

For pelletization, 10 % polyvinyl alcohol (PVA) was added as a binding medium to the ground calcinated powder. This powder was placed in a die and an MTI compact hydraulic pellet press for 5 mins under a load of 1.5 tons. The green pellet was 8 mm in diameter and approximately 1 mm in thickness. Different green pellets were sintered at 800 °C for different times of 3 h, 6 h, 12 h, and 24 h. For the sintering process, the ramp-up rate was 5 °C/min. Moreover, to ensure complete removal of the binding medium, the temperature was held at 500 °C for 30 mins.

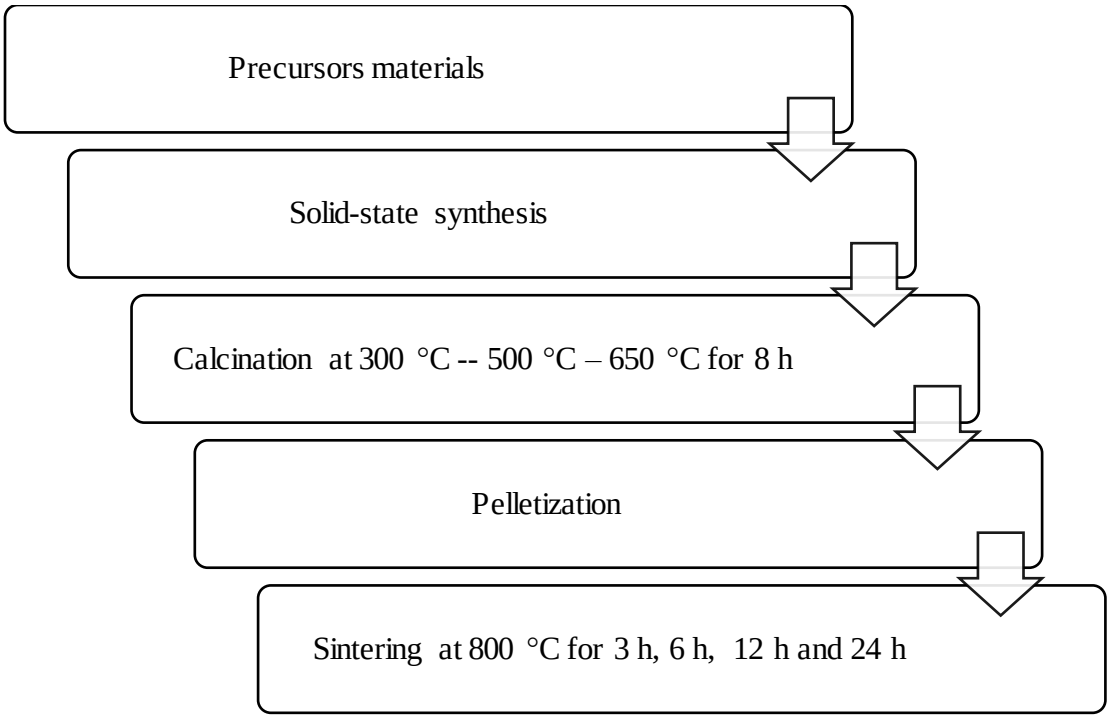

Figure 3.1: Solid State Reaction.

3.2 PULSED LASER DEPOSITION (PLD)

The LGP films were deposited using PLD. PLD is a physical vapor deposition (PVD) technique. It uses a high-power pulsed laser beam which is focused inside a vacuum chamber to strike the target of the material that is to be deposited. Vaporized material from the target forms a plasma plume that is deposited on a substrate as a thin film. These depositions are usually done in the presence of a background gas or vacuum. [48] COMPex Pro, an excimer laser from COHERENT, was used in our setup. The term excimer refers to an excited dimer (diatomic molecule formed by the union of two atoms). The molecules used contain noble gases, which under normal circumstances, do not form a compound. However, they have an excited state where they are temporarily bonded as they have no stable ground state. In the case of a krypton fluoride excimer laser, a pulsed electrical charge excites the molecule, which results in the formation of a metastable excited state KrF*. After a short time, it disassociates according to the following reaction

$$KrF^* \longrightarrow Kr + F + h\nu \quad (2)$$

where hν represents the photon of wavelength 249 nm. [49]

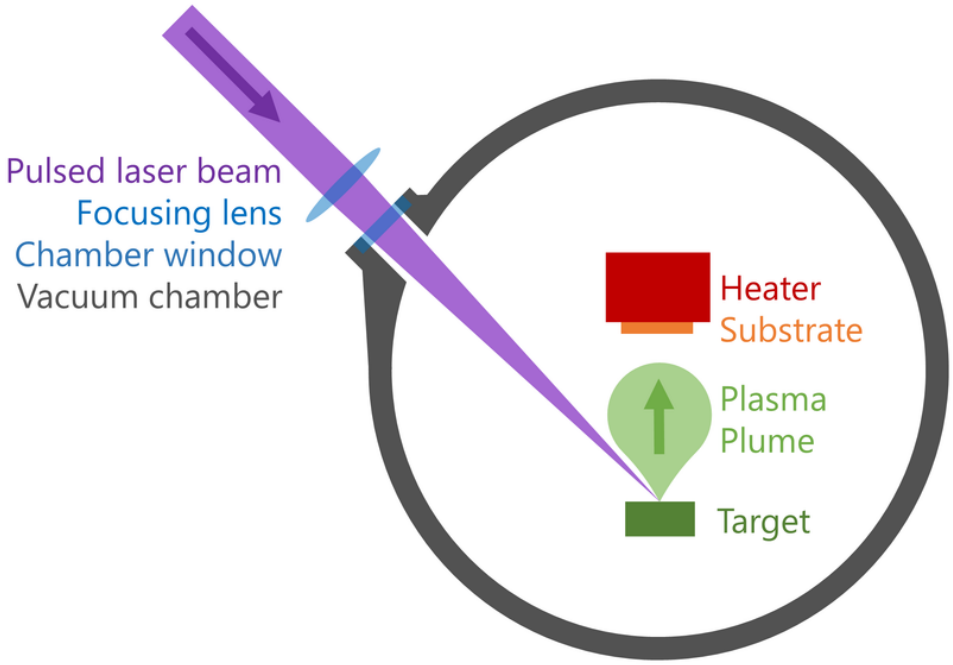

Figure 3.2: Schematic diagram of the PLD chamber setup (Tedsanders from Wikipedia).

The LGP films were grown in a stainless steel high-vacuum chamber, and its schematic representation is shown in Figure 3.2. The chamber was pumped down to a base pressure of 7.2 E-3 mTorr (high vacuum) and then filled up by oxygen to maintain a constant working pressure of 50 mTorr. Throughout the experiment, the laser was pulsed at a repetition rate of 5 Hz for 2000 pulses with a pulse energy of 220 mJ. The ceramic target was prepared in the exact procedure as pellets with the sintering conduction being 800 °C for 12 h. However, the die used for the target was of 25 mm diameter, and the resulting thickness was 7 mm. The films were deposited onto Si (100) wafers.

Table 3.1: Substrate temperature of thin films fabricated

Substrate Temperature
RT
400 °C
500 °C
550 °C
600 °C
650 °C
700 °C

3.3 X-RAY DIFFRACTION (XRD)

For characterizing crystalline materials, XRD is one of the most powerful non-destructive technique (NDT) available. It provides information such as structures, phases, preferred crystal orientations, average grain size, and crystallinity. A monochromatic beam of X-rays is scattered at specific angles from each set of lattice planes, which results in constructive interference and produces XRD peaks. Thus, atomic positions determine the peak intensities. Hence, XRD is unique and can enable quick phase identification utilizing a standard database.[50] However, in the case of thin films, this technique is susceptible to substrate interference. Hence grazing incidence x-ray diffraction (GIXRD) was used, which has a small angle of incidence on the sample surface.

Bragg's law relates these diffraction patterns with the crystalline plane as

$$n\lambda = 2d\sin\theta \quad (3)$$

where n is an integer, λ is the wavelength of the incident radiation, d is the inter-planar atomic distance, and θ is the angle of diffraction.

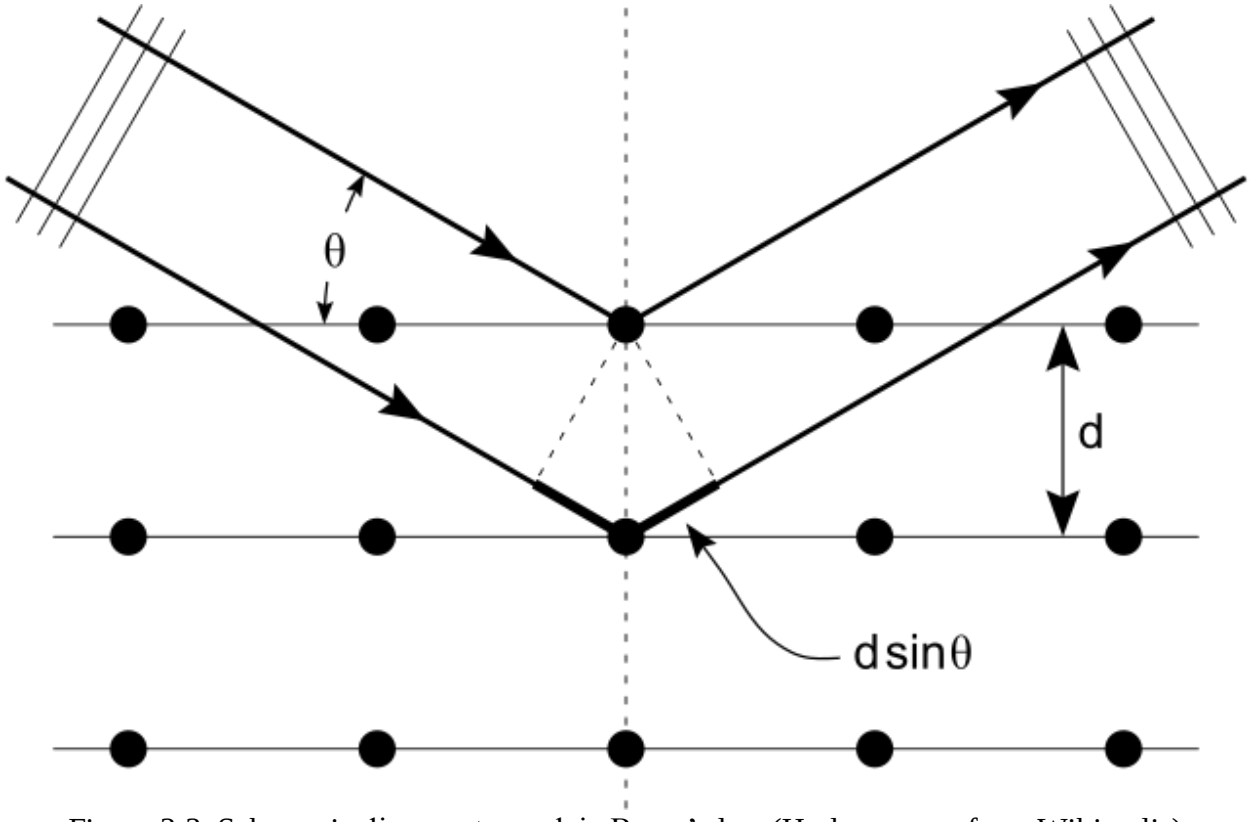

Figure 3.3: Schematic diagram to explain Bragg's law (Hydrargyrum from Wikipedia)

A Rigaku Benchtop powder XRD-Mini Flex II equipped with Cu Kα radiations (λ= 1.54056 Å) was used to measure the powder LGP samples. Measurements were taken at room temperature in the 2θ range of 10° to 80° (step size of 0.02°) with a scan rate of 1°/min. High-resolution XRD scans were performed with a scan rate of 0.116°/min for Rietveld refinement. For thin films, Rigaku Smartlab equipped with Cu K_α radiations (λ= 1.54056 Å) was used for theta/2-theta measurements at room temperature in the 2θ range of 10° to 80° (step size of 0.01°) with a scan rate of 1°/min.

3.4 SCANNING ELECTRON MICROSCOPY (SEM)

Scanning electron microscopy (SEM) is an indispensable tool for the characterization of materials from nanometer to micrometer scale [51]. A focused beam of electrons scans the surface

on the sample to produce an image. Information about the surface topography and composition of the sample is present in the various signals resulting from the electrons interacting with atoms in the sample. The electron source used in the SEM can be a tungsten filament, LaB_6, Schottky emitter, or a tungsten field-emission tip. Furthermore, these are typically smaller compared to transmission electron microscopy (TEM) as the maximum accelerating voltage (typically 30 kV) is lower.

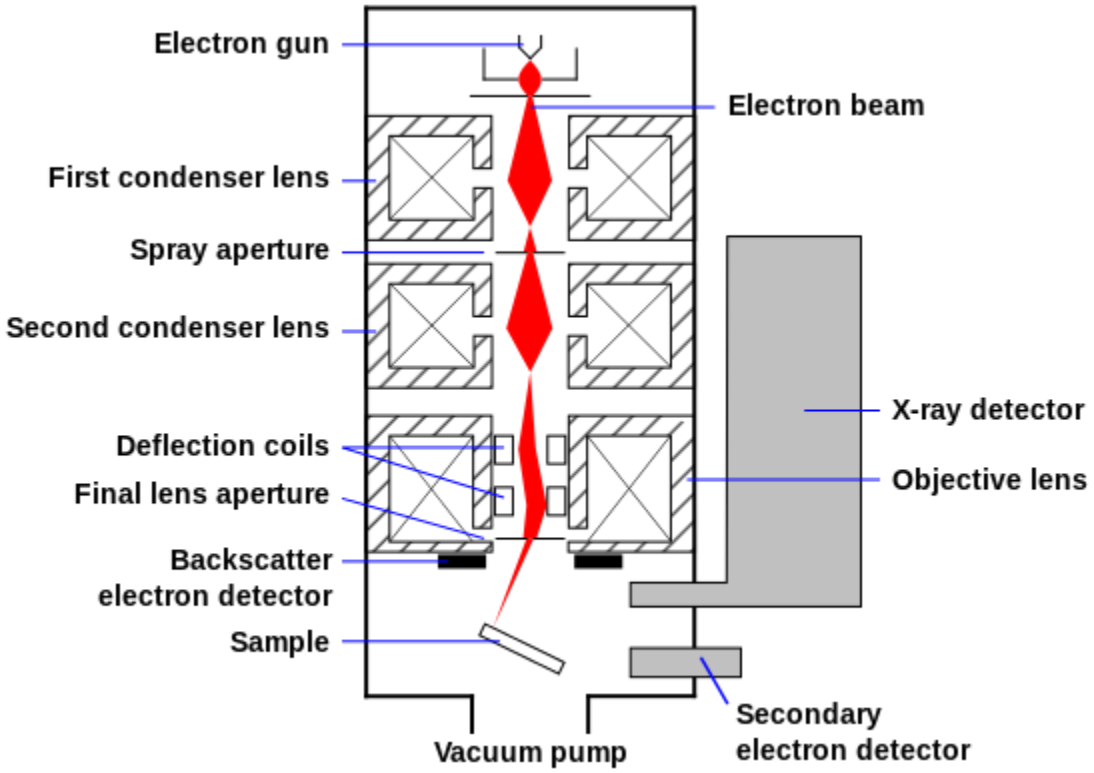

Figure 3.4: Schematic representation of SEM (Steff, ARTE and MarcoTolo from Wikipedia).

Due to the interaction of the electron probe with the sample surface, the various signals produced include characteristic X-rays (generated by excitation of inner shell electrons), cathodoluminescence (excitation in the range of visible light that is associated with valency electron excitation), backscattered electrons (elastically scattered out of the surface) and secondary electrons (inelastically scattered ejected from the surface of the target). Secondary electrons are low in energy but high in number and are emitted from a region that is highly localized at the point

of impact of the probe. Therefore, they are readily detected and can form an image. Its potential resolution is limited primarily by the diameter of the focused probe at the sample surface. [51]

A Hitachi S-4800 (field-emission scanning electron microscopy) SEM was used to look at the surface morphology of the pellets. The SEM sample was prepared by sputter coating a thin layer of gold in an Argon (Ar) atmosphere using an SPI sputter coating module to avoid charging problems. The images were taken using the electron beam energy set at 5 kV. As for the thin film measurements, a FEI Magellan 400 SEM was used. The source in this SEM is a Schottky thermal emission source. Images were taken using an electron beam energy of 5 kV.

3.5 Dielectric Measurements

Dielectric properties of material include dielectric constant and dissipation factor. The dielectric constant is usually used to describe the dielectric characterization of a material and is one of the critical parameters to consider for a capacitor material. The higher the dielectric constant and dissipation factor, the more energy is absorbed from an electric field [52].

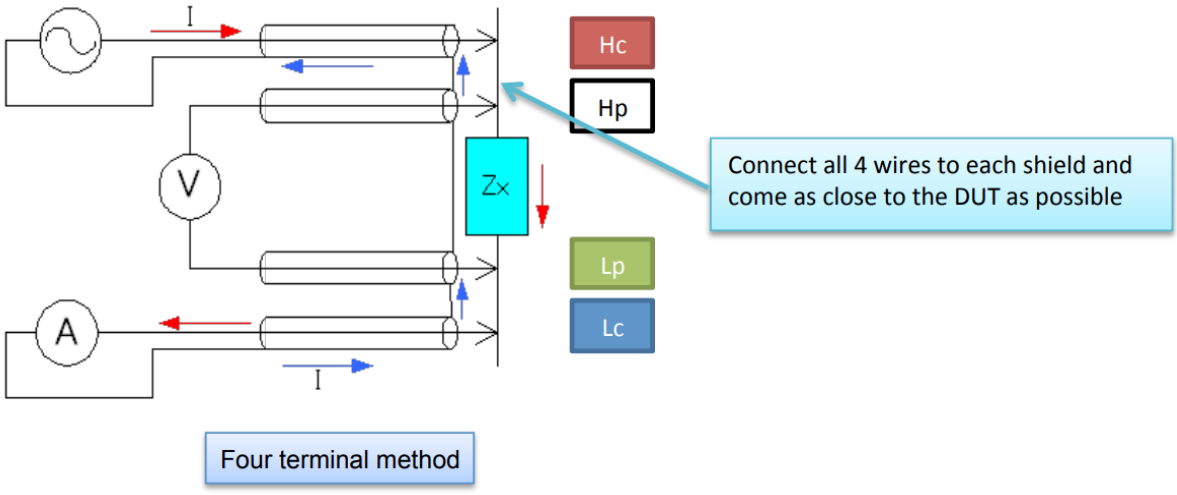

Figure 3.5: Schematic representation of 4 terminal method [53].

Hioki IM3536 LCR meter was employed for dielectric property measurements. Accuracy of the readings was ensured by performing circuit corrections and collecting data after the warmup

period of the equipment. Furthermore, 4 terminal method was used to measure data, the schematic shown in Figure 3.5. The LGP sample was prepared by fine polishing and coating with a thin layer of silver (Ag) paint on both sides of the pellet. The sample was baked at 90 °C for 2 h. The pellet served as a dielectric and the silver paint as the metal electrodes in a capacitor. The capacitance, dielectric loss (tan δ), and inductance data were taken over a frequency range of 1 kHz to 1 MHz up to 500 °C from room temperature.

3.6 ELLIPSOMETRY

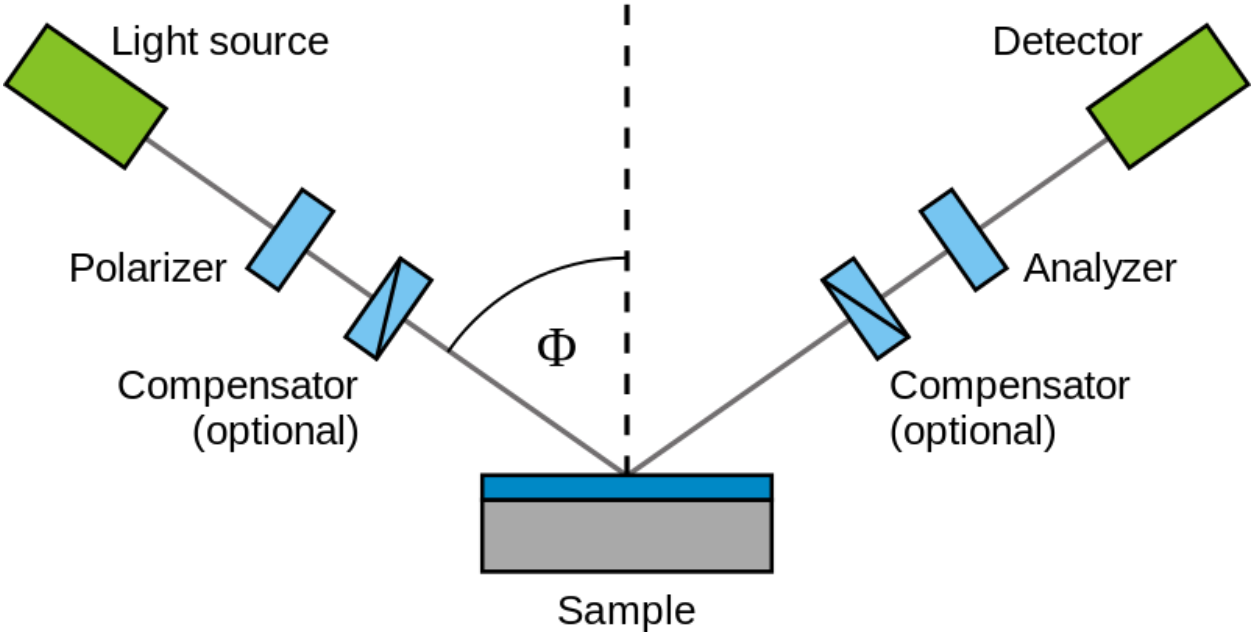

Figure 3.6: Schematic setup of ellipsometry experiment (Buntgarn and Stannered from Wikipedia).

Ellipsometry is an indirect optical technique as information about the properties of a sample is obtained through modeling analysis. [54] The utilization of this technique measures the relative change in amplitude and phase for the linearly polarized monochrome incident light as it is obliquely reflected from the sample surface.

A SE-2000 spectroscopy ellipsometer from SEMI lab was used to measure the optical properties of the LGP thin film. Measurements were taken in the range of 350-1200 nm wavelength at incident angles of 65º, 70º, and 75º, near the Brewster's angle of silicon. The data analysis was performed using SEA software package from SEMI lab.

3.7 SECOND HARMONIC GENERATION (SHG) MICROSCOPY

SHG microscopy is a nonlinear imaging technique. It is a two-photon coherent nonlinear optical process that arises from polar molecules ordered in noncentrosymmetric assemblies [55]. It is based on a nonlinear optical effect known as second-harmonic. In this process, two photons with the same frequency interact with a nonlinear material and generate a new photon with twice the energy of the initial photons. This is equivalent to the new photon having twice the frequency and half the wavelength compared to the initial photon. Hence, it is also called frequency doubling. This technique is extensively used in the visualization of cells and tissues.

A two-photon microscope developed and built earlier by the UTEP Photonics Laboratory [56–58] was used to probe the nonlinear optical properties of LGP thin films. Second-harmonic generation (SHG) microscopy images were captured for the analysis of SHG power and SHG polarization scans. The laser source used had a wavelength of 950 nm (Mai Tai HP, Spectra-Physics), while the samples were focused on a 60x water-immersed objective (Olympus LUMPlanFL N 60x/1.00 W) and the blue channel (417–477 nm) was used for analysis. Each image produced was a result of a combination of fifty frames. Image were analyzed on ImageJ and the data was plotted on OriginPro 8.5. An adhesive tape was used to hold each sample on a glass slide with coverslip for imaging.

Power scans were performed by varying laser power manually using optical attenuator and were metered before entering the instrument for imaging. Power was increased in +5 mW

increments from 1 mW until it was sufficient to saturate the blue channel. The 700°C sample was imaged until power of 165 mW (34 images) , room temperature sample until 180 mW (37 images), and 500°C sample until 120 mW (25 images).

A half-wave plate (HWP) filter was employed for polarization scans. It was introduced into the path of the beam path, which polarized incident light linearly. The HWP was manually rotated at increments of +5° from 0°–180° (37 images) in a 0°–360° polarized light. Power used for the 700°C and RT samples was 150 mW, while the 500°C was 90 mW.

Chapter 4: Results and Discussion

4.1 Structure and Morphology of LGP Ceramics

The XRD data of LGP ceramics are shown in Fig. 4.1. The XRD data of 300 °C calcinated sample indicates the presence of unreacted secondary phases (marked by a black star in Figure 4.1, and thus, calcination was repeated at a higher temperature of 500 °C. Although the XRD of the 500 °C calcinated sample shows a decrease in the quantity of unreacted secondary phase, it is still present in significant amounts (marked by a red star in Figure 4.1. After the third step of calcination at 650 °C, XRD obtained matches XRD from the literature [37]. The peaks were successfully indexed in monoclinic system with $P2_1$ space group.

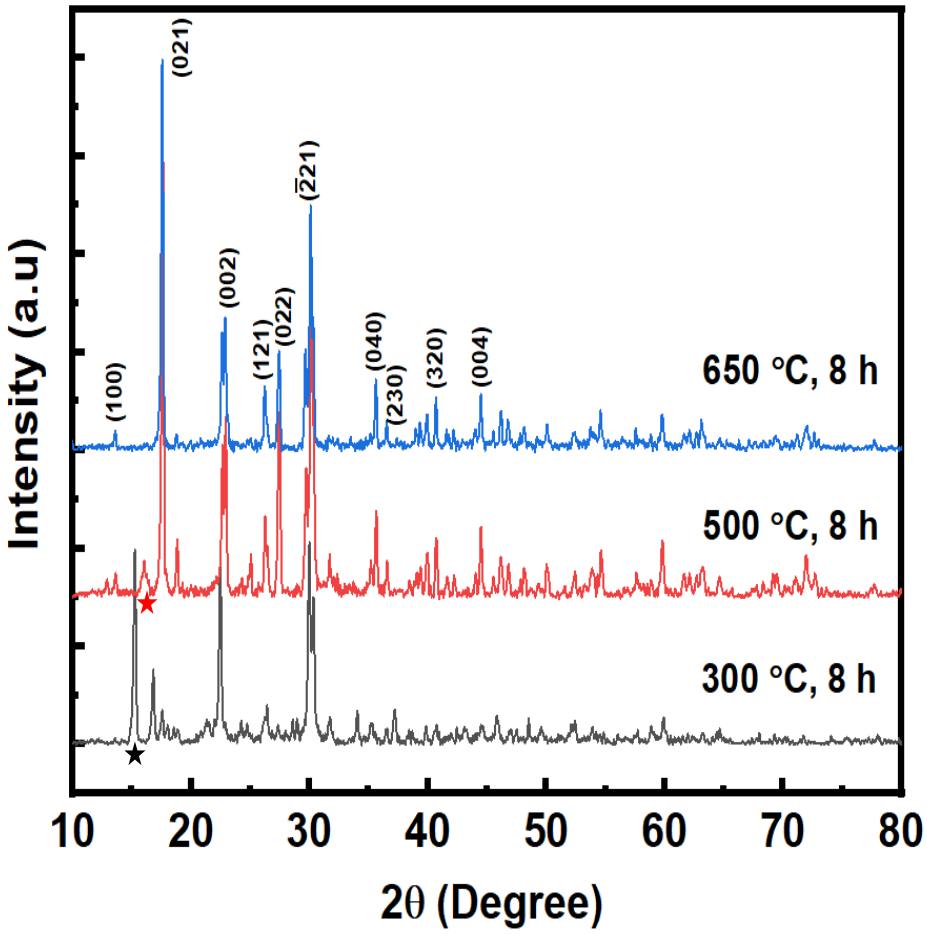

Figure 4.1: X-ray diffraction patterns of sample calcined at different temperatures.

To further understand the effect of sintering time on the structure and phase stability of LGP ceramics, XRD analysis of the ceramics was performed as a function of sintering time. The data are presented in Figure 4.2. The XRD patterns collected from sintered samples indicates a peak shift to the left with an increase in sintering time, and this suggests change in lattice parameters. It is visible in the expanded view in Figure 4.2.

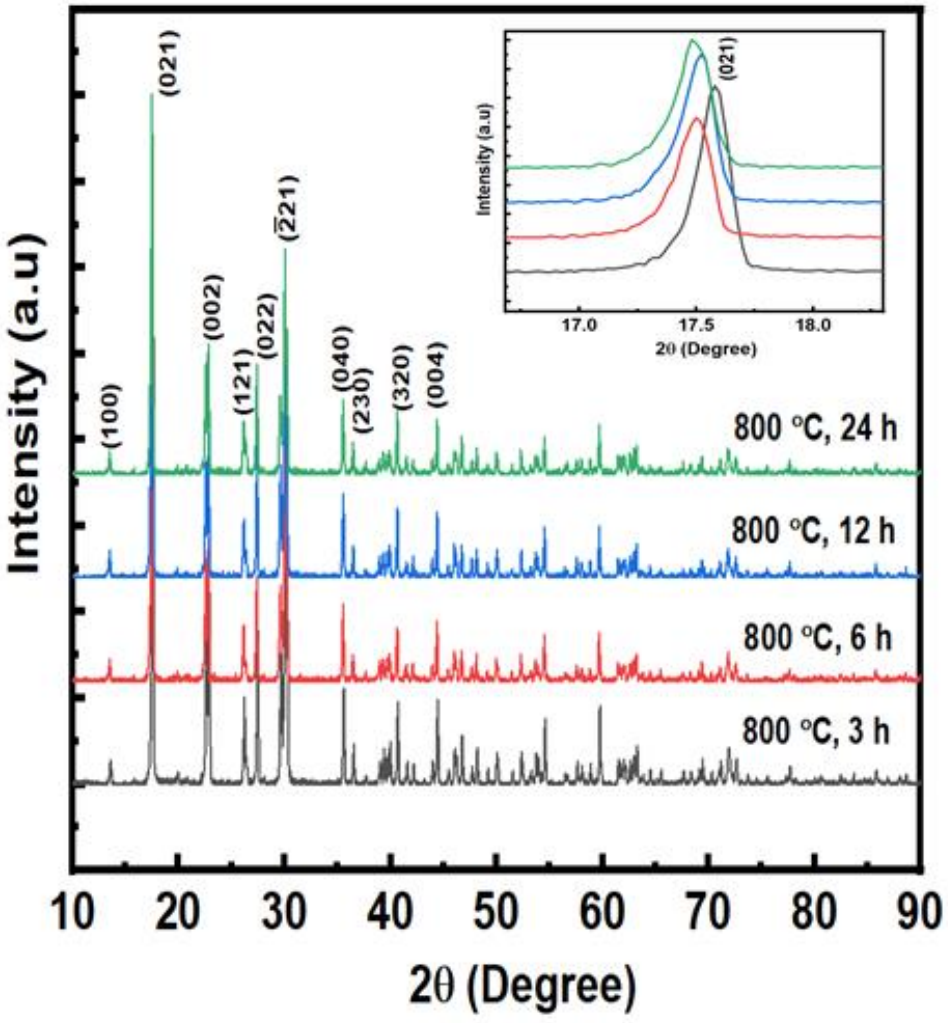

Figure 4.2: XRD patterns of sample calcined at different times.

The crystallite size of the LGP samples was estimated using the Debye Scherrer equation [59]:

$$D = \frac{K\lambda}{\beta \cos\theta} \quad (4)$$

where D is the average crystallite size of the sample, K is shape factor (0.9), λ is the wavelength of X-ray source (1.54056 Å [Cu K_α]), β is full width at half maximum (FWHM) and θ is angle corresponding to β. The seven most intense peaks (17.56°, 22.65°, 22.89°, 26.23°, 27.46°, 29.67851°, and 30.14°) were fitted using the Gaussian function to obtain the FWHM and its corresponding 2θ values. Gaussian function gave the best fit for all XRDs. The crystallite size variation is as presented in Table 4.1.

Table 4.1: Crystallite size of LGP samples

LGP Sample	Crystallite size (nm)
800 °C, 3 h	48.6138
800 °C, 6 h	51.8912
800 °C, 12 h	52.5967
800 °C, 24 h	48.6737

The crystallite size increases when sintering time increases from 3 h to 12 h. Moreover, the change in size from 3 h to 6 h is substantially greater than from 6 h to 12 h. However, there is a decrease in crystallite size when sintering time is increased to 24 h. This suggests the prevention of crystal growth with an increase in temperature.

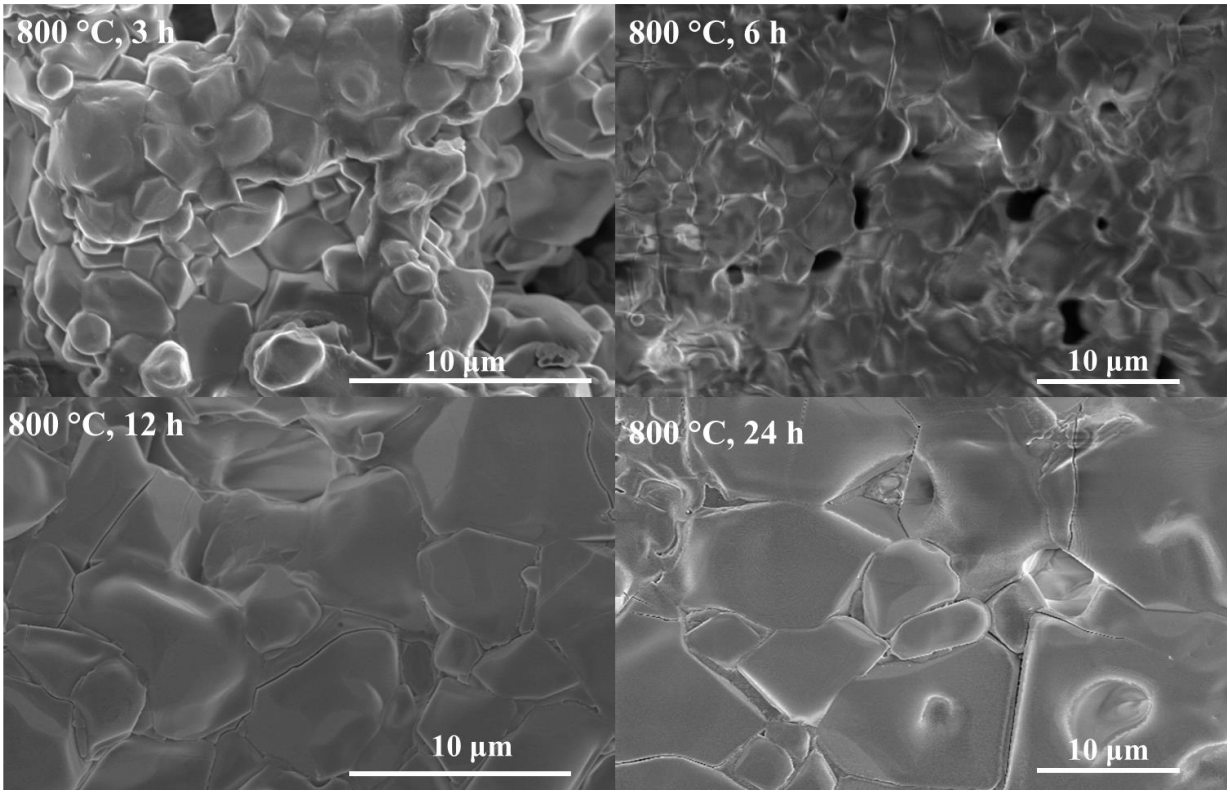

Figure 4.3: Scanning Electron Microscope images of samples sintered at 800 °C with varying sintering time.

The increase in grain size is visually evident from the SEM images with the increasing of sintering time. Furthermore, there is a distinct change in the 24 h sintered sample, this could be due to the volatile nature of Li based compounds. To quantify grain size, we utilize the intercept method to calculate grain size. The equation utilized was:

$$\text{Average grain size} = \frac{\text{Line Length}}{\text{No. of Intercepts}} \quad (5)$$

To ensure accurate values multiple SEM images from different parts of the pellet was used for every sintering time on ImageJ. Furthermore, porosity was also calculated utilizing these images. The increase in sintering time decreases the porosity of the sample while also increasing the average particle size.

Table 4.2: Average particle size and porosity of samples

LGP Sample	Porosity (%)	Average Particle Size (µm)
800°C 3 h	3.815	1.7194
800 °C 6 h	2.131	3.879
800 °C 12 h	0.441	4.084
800 °C 24 h	0.176	6.994

4.2 RIETVELD STRUCTURAL REFINEMENT

Rietveld method is a refinement technique and not a structure solution method. Therefore, it requires a good starting model. The goal of this method is to minimize the residual function using a nonlinear least-squares algorithm and thus refine the structure.

$$\mathrm{WSS} = \sum_i w_i (I_i^{exp} - I_i^{cal})^2 , w_i = \frac{1}{I_i^{exp}} \quad (6)$$

The model utilized was from the literature [37]. XRD data ensures that there was no secondary phase. The refinement was undertaken considering the monoclinic crystal symmetry with $P2_1$ space group. For refined experimental diffraction patterns, pseudo-Voigt peak shape function was used. The obtained goodness of fits is also shown in Figure 4.5, and the refined unit cell parameters are presented in Table 4.3. Refined cell parameters indicate a small decrement in unit cell volume associated with the increase in sintering time of the LGP sample.

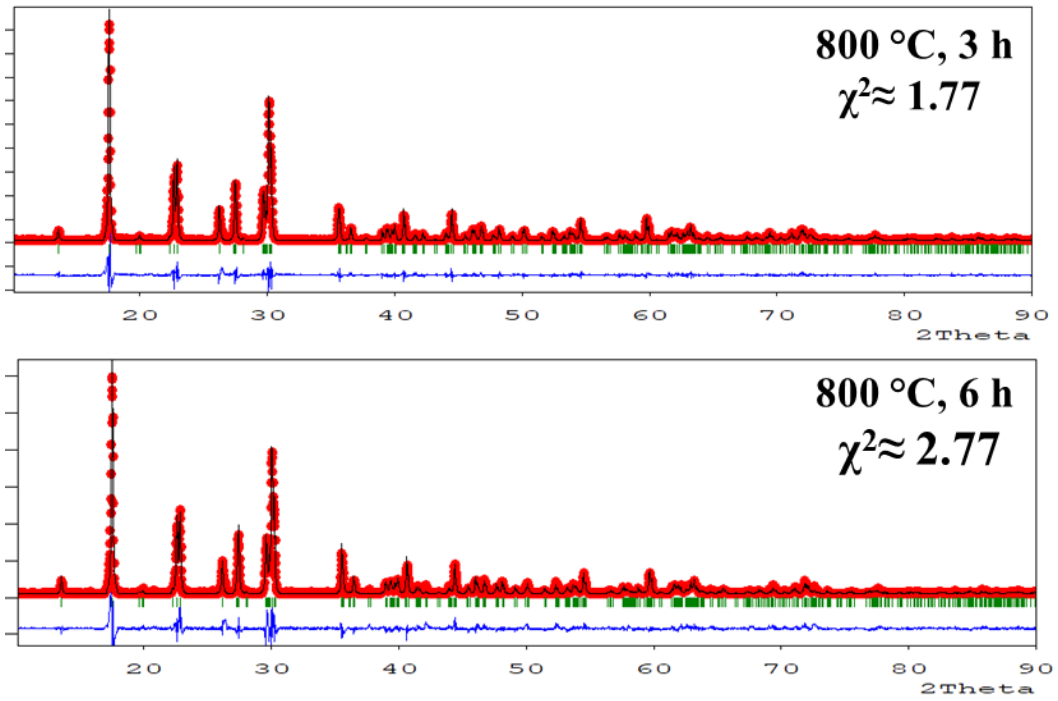

Figure 4.4: Rietveld structural refinement of XRD patterns for LGP samples sintered at 800 °C for 3 h and 6 h.

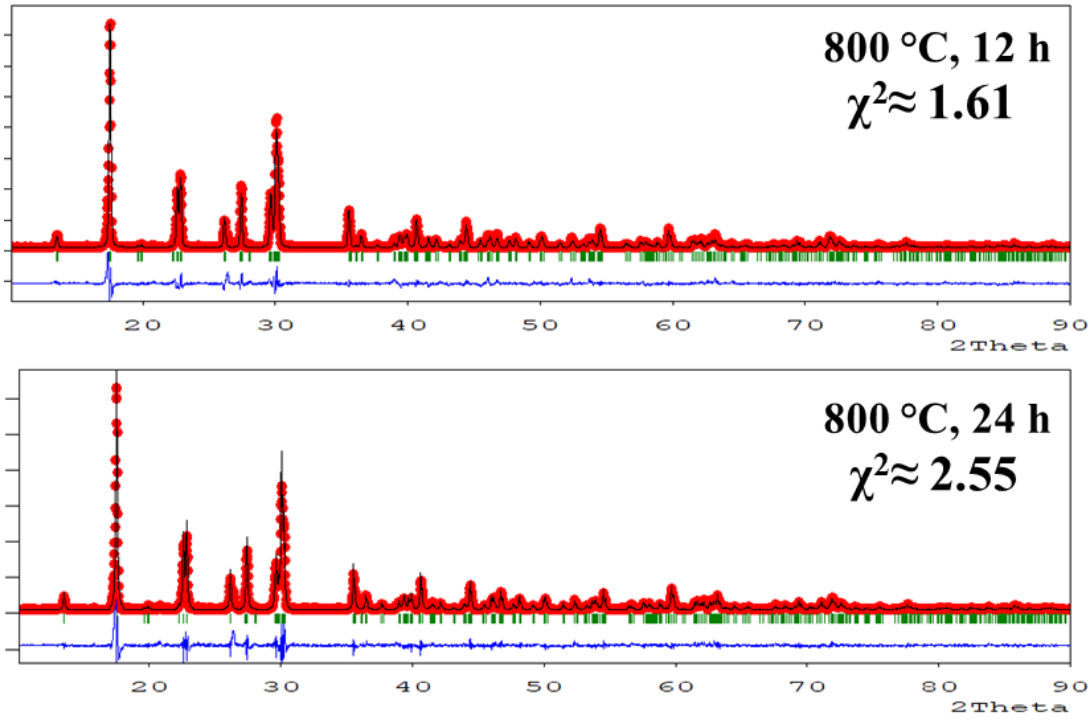

Figure 4.5: Rietveld structural refinement of XRD patterns for LGP samples sintered at 800 °C for 12 h and 24 h.

Table 4.3: Refined unit cell parameter and volume of unit cells

LGP	a (Å)	b (Å)	c (Å)	β (°)	Volume (Å^3)
Literature	4.7593	7.9586	6.8940	109.06	246.81
800°C 3 h	4.7632	7.95859	6.88341	109.0043	246.7161
800°C 6 h	4.76318	7.95921	6.88278	109.00897	246.7047
800°C 12 h	4.76266	7.95737	6.88192	109.0133	246.5835
800°C 24 h	4.76198	7.95809	6.88129	108.99638	246.5731

4.3 DIELECTRIC PROPERTY ANALYSIS

The sintered LGP sample was exposed to a frequency sweep from 1kHz to 1MHz at every 10 °C from room temperature to 500 °C. The capacitance (C), dielectric dissipation (tan δ) and inductance (Z) were recorded. For energy applications, capacitance is an essential factor. Geometry and dielectric constant determine the capacitance of the material.

$$C = \frac{\varepsilon' \varepsilon_0 A}{t} \tag{7}$$

where ε' is the real part of the dielectric constant, ε_0 is the dielectric constant of free space (8.85×10^{-12} F/m), A is the area of capacitor plate, and t is the thickness of the pellet.

The dielectric dissipation of the material is defined as

$$\tan \delta = \frac{\varepsilon''}{\varepsilon'} \tag{8}$$

where, $\varepsilon''$is the imaginary part of the dielectric constant.

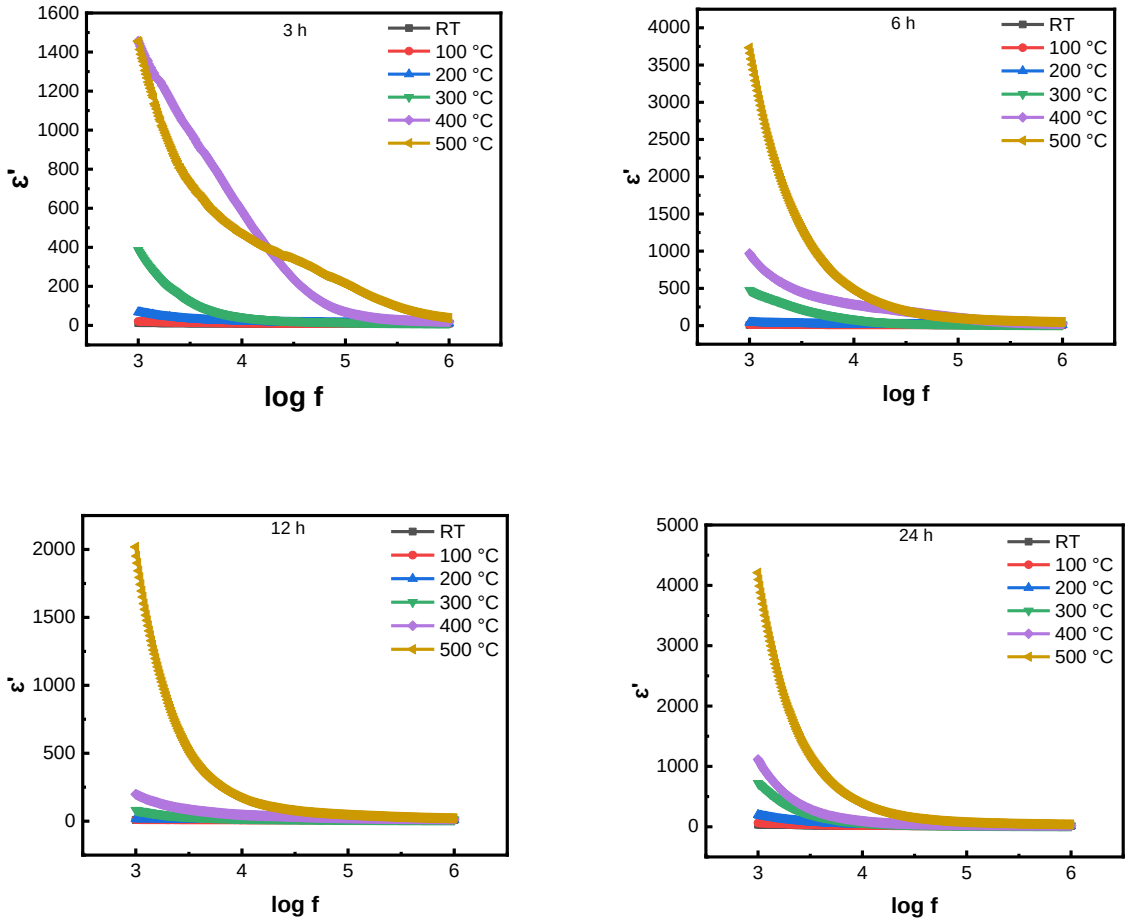

Figure 4.6: Frequency dependence of the real part of dielectric constant (ε') at different temperatures for LGP sample sintered at 3 h, 6 h, 12 h, and 24 h.

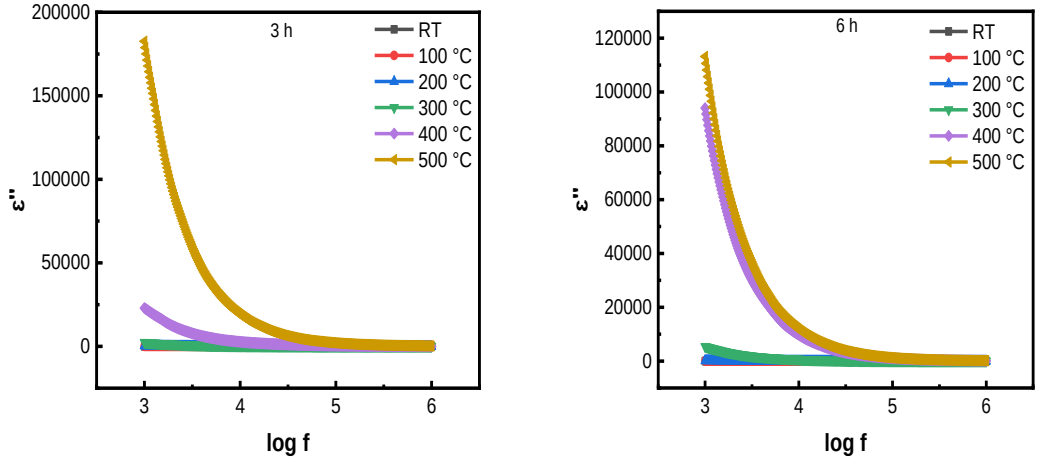

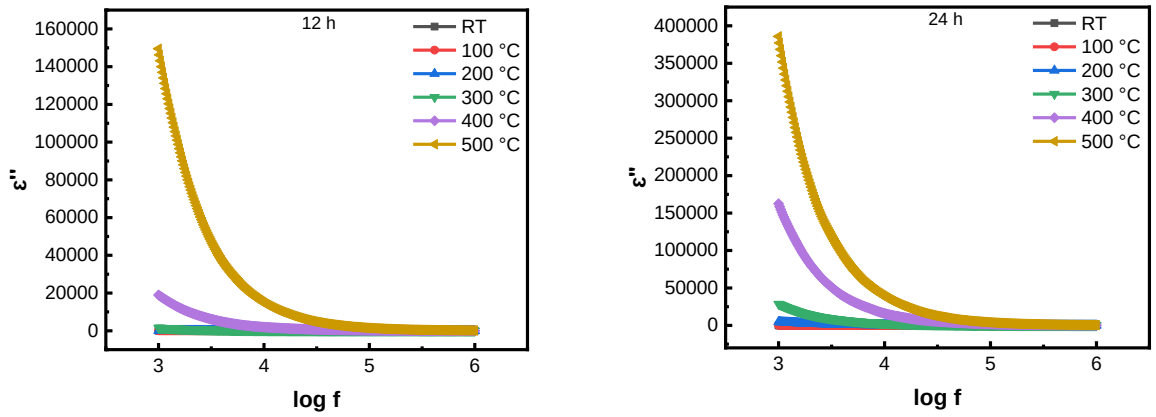

Figure 4.7: Frequency dependence of the imaginary part of dielectric constant (ε″) at different temperatures for LGP sample sintered at 3 h, 6 h, 12 h, and 24 h.

Figure 4.6 and Figure 4.7 indicates that, at a given temperature, the dielectric constant decreases with increasing frequency and reaching an almost constant value at higher frequencies. This typical behavior of dielectric constant with frequency and can be explained by considering various polarization sources and associated mechanisms [60]. At lower frequencies, due to the contributions from various polarizations such as interface, space charge (where potential barriers lead to charge accumulation), and ionic charges leads to larger dielectric constant. At higher frequencies, electric dipoles fail to orient themselves due to the fast variation of applied electric field and current, thus lagging and resulting in low dielectric values [61]. In the lower frequency range, electric dispersion is attributed to interfacial polarization as the electronic and atomic polarizations remain for the majority unchanged [62]. This behavior can be explained by Maxwell–Wagner theory of interfacial polarization [63], following Koops phenomenological theory [64,65].

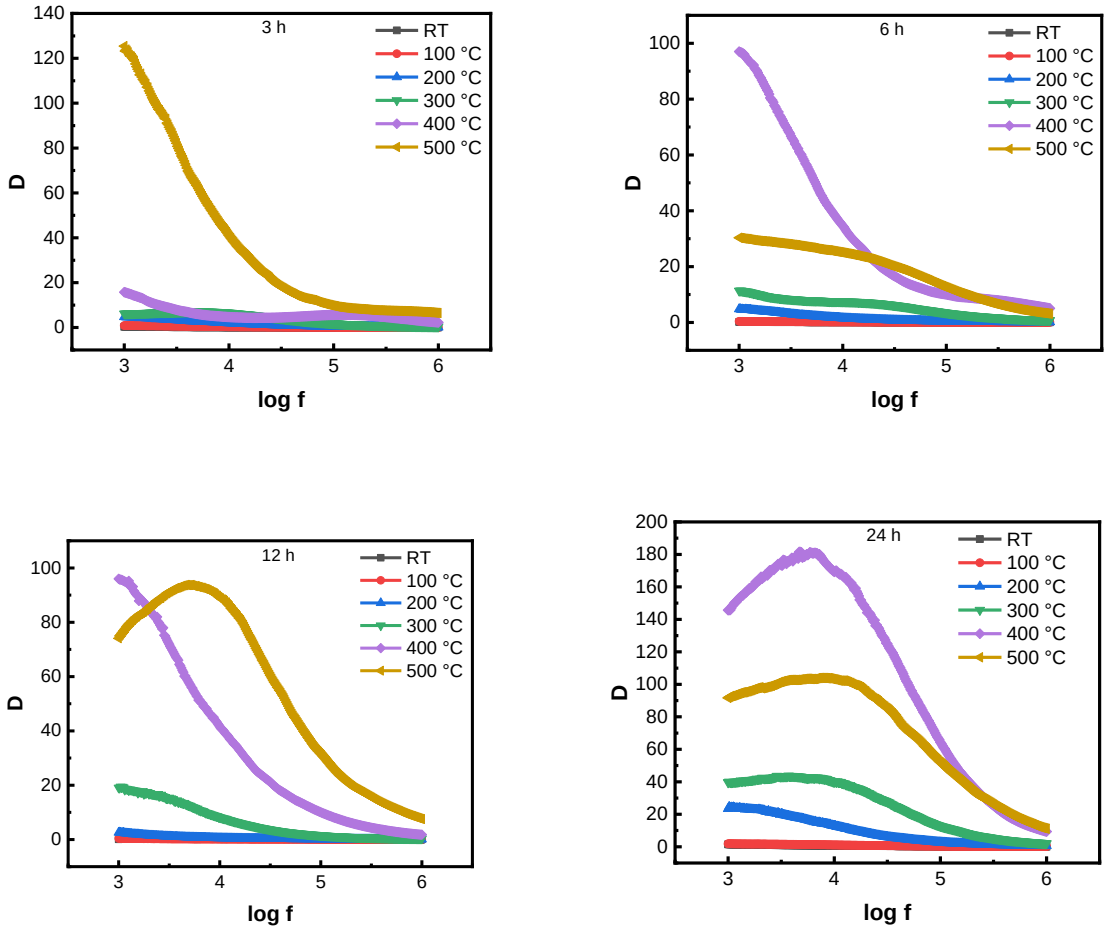

Figure 4.8: Frequency dependence dielectric loss at different temperatures for LGP sample sintered at 3 h, 6 h, 12 h, and 24 h. The phase difference between the applied electric field and the induced current is D or δ [66].

The dielectric dissipation values decrease with increasing frequency (Figure 4.8) at higher temperatures. However, at a lower temperature, it remains nearly constant throughout the entire frequency sweep.

LGP has multiple ion species present, and thus it would be necessary to observe the dispersion behavior using the Debye function [67,68]. In this real part of the dielectric at a given angular frequency (ε' (ω)) is defined by the following relation:

$$\varepsilon'(\omega) = \varepsilon_{\infty} + \frac{(\varepsilon'_0 - \varepsilon'_{\infty})}{[1+(\omega\tau)^{2(1-\alpha)}]} \quad (9)$$

where ε'_0 is the real part of the dielectric at low frequency (1kHz for us), ε'_∞ is the real part of the dielectric at high frequency (1MHz for us), ω is the angular frequency (=$2\pi f$), τ is the Debye average relaxation time, α is the spreading factor for actual relaxation time about the mean value and ε_∞ is the complex dielectric at high frequency (1MHz for us).

In order to obtain τ and α the Cole-Cole plot was employed [67]. In this, Equation 4.5 was utilized with a slight modification of using the real part of the dielectric at high frequency rather than the complex dielectric at high frequency (modified Debye's function) to obtain the following equation:

$$y = \ln\left(\left|\frac{(\varepsilon'_0 - \varepsilon')}{(\varepsilon' - \varepsilon'_\infty)}\right|\right) = 2(1-\alpha)\ln\omega + 2(1-\alpha)\ln\tau \qquad (10)$$

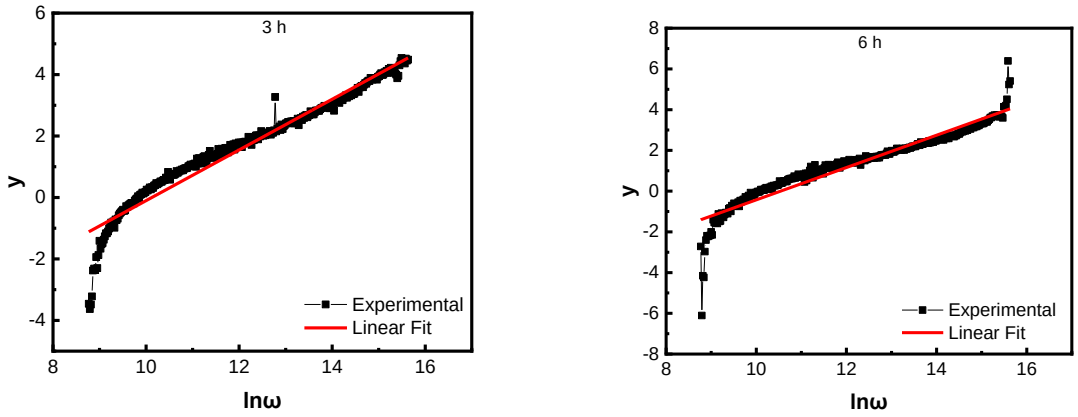

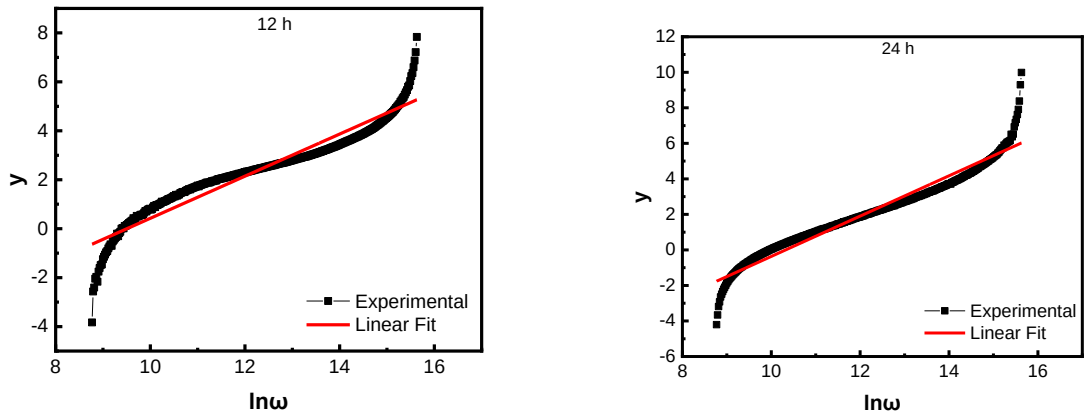

Figure 4.9: Variation of ln $\left(\left|\frac{(\varepsilon'_0-\varepsilon')}{(\varepsilon'-\varepsilon'_\infty)}\right|\right)$ with angular frequency for LGP sample sintered at 3 h, 6 h, 12 h, and 24 h.

A linear fit was employed to obtain the slope and intercept (Figure 4.9), and based on Equation 6, α and τ values were calculated. Utilizing the α and τ obtained, ε'(w) was calculated and plotted (Figure 4.10).

Table 4.4: Spreading factor and relaxation time determined using Cole-Cole plots

LGP Sample	Spreading Factor, α	Relaxation Time, τ (μs)
800 °C, 3 h	0.59585	36.42
800 °C, 6 h	0.61100	27.10
800 °C, 12 h	0.50376	11.60
800 °C, 24 h	0.44400	33.70

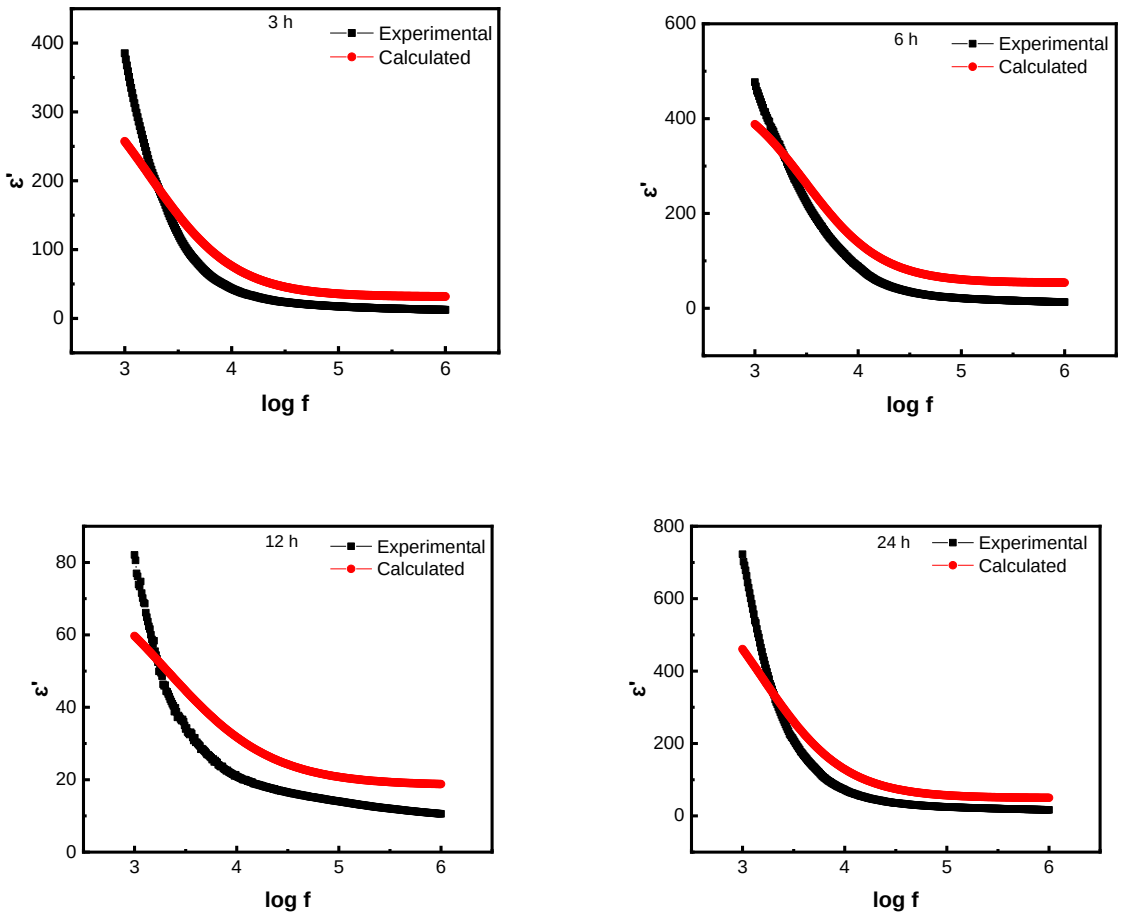

Figure 4.10: Variation of the real part of the dielectric constant and real part of dielectric constant fitted to modified Debye's equation with frequency for LGP sample sintered at 3 h, 6 h, 12 h, and 24 h.

Figure 4.10 shows that the experimental and calculated values are consistent, especially at higher frequencies. Thus, proving the validity of modified Debye's equation and the possibility that multiple ions contribute to the dielectric relaxation process [61]. Furthermore, we notice that the rate of decrease of the dielectric at lower frequencies is much higher compared to higher frequency. It is likely caused by polarization of interface and grain boundaries or intrinsic factors

like ionic, electronic, and space charge polarization. Thus, this behavior can be explained due to various polarization sources [60].

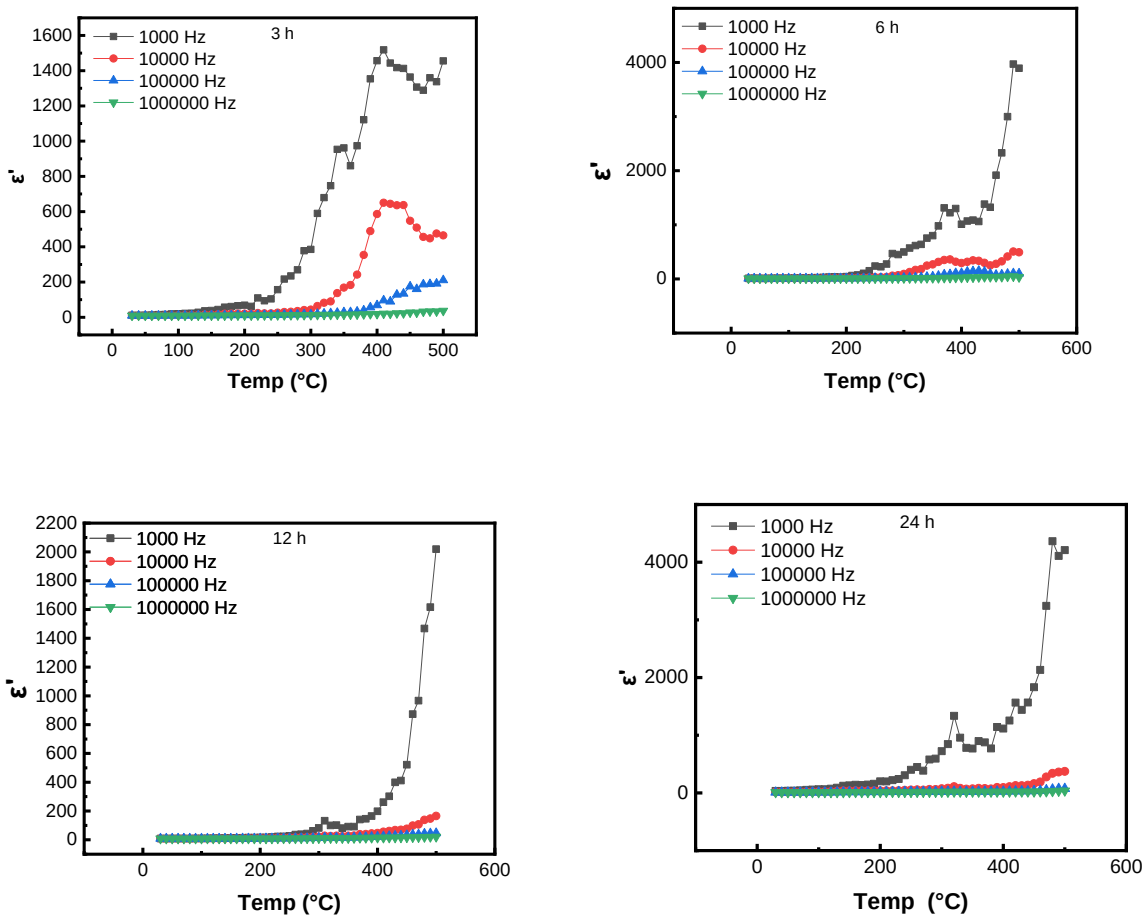

Figure 4.11: Temperature dependence of the real part of dielectric constant at different frequencies for LGP sample sintered at 3 h, 6 h, 12 h, and 24 h.

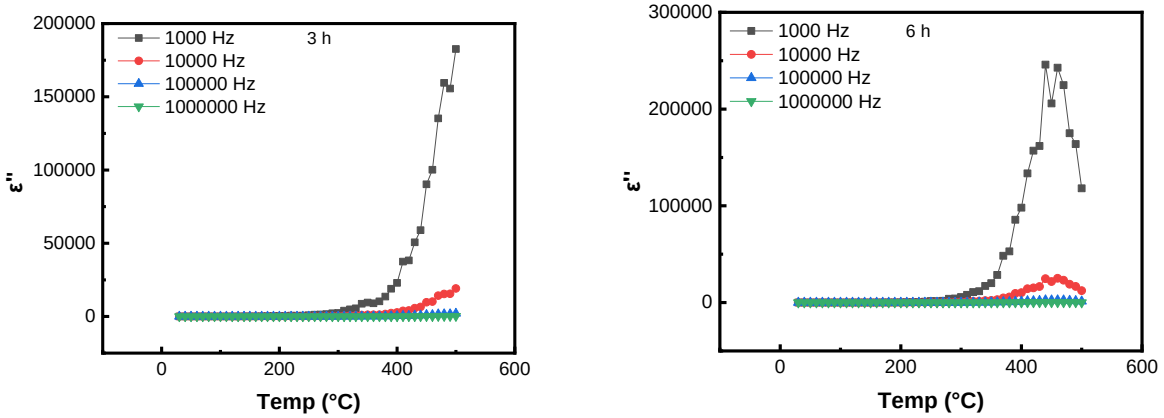

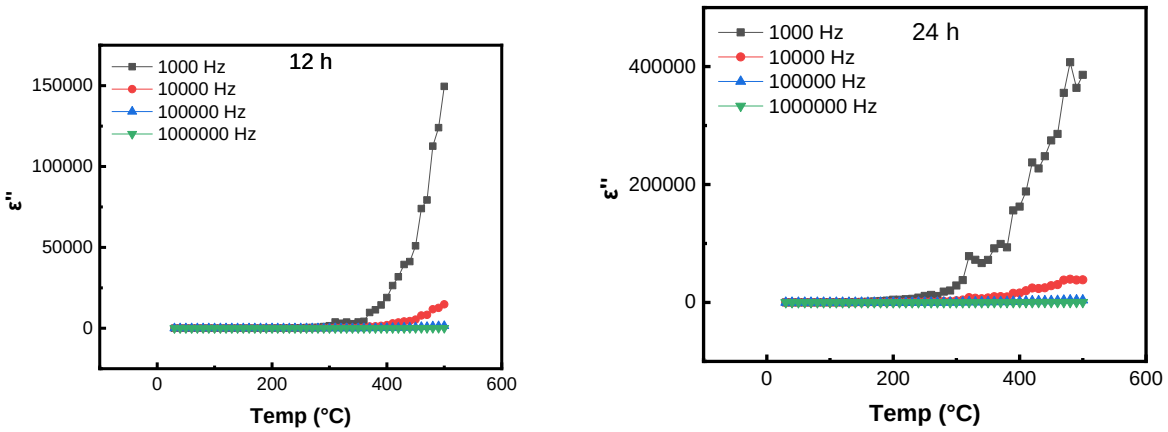

Figure 4.12: Temperature dependence of the imaginary part of the dielectric constant at different frequencies for LGP sample sintered at 3 h, 6 h, 12 h, and 24 h.

The temperature dependence of dielectric constant has been studied to further understand the properties of the LGP samples and their dielectric relaxation processes/behavior. The dielectric constant and loss have been plotted against temperature at 1 kHz, 10 kHz, 100 kHz, and 1 MHz. From Figure 4.11 and Figure 4.12, we see that dielectric constant remains the same until around 250 °C to 300 °C and then increases as temperature increases. This behavior is more clearly seen at lower frequencies (1 kHz and 10 kHz) compared to the higher frequencies (1 MHz). Furthermore, the LGP sample sintered at 800 °C for 3 h, shows dielectric relaxation around 420 °C for both 1 kHz and 10 kHz. However, relaxation is absent from the other samples in our range of measurements.

The increase of dielectric constants at higher temperatures is a result of thermal energy increasing mobility of charge carriers and boosted the hopping rate of charge carriers. The dielectric constants at lower frequency are larger than the higher frequency as there is less lagging between applied electric field and current and various polarization sources, resulting in higher values. As temperature increases, the effect of space charge polarization increased, which explains

the increase in dielectric dissipation shown in Figure 4.13. Furthermore, there is a sharp decrease in dielectric dissipation around 430 °C for samples sintered at 800 °C for 6 h, 12 h, and 24 h.

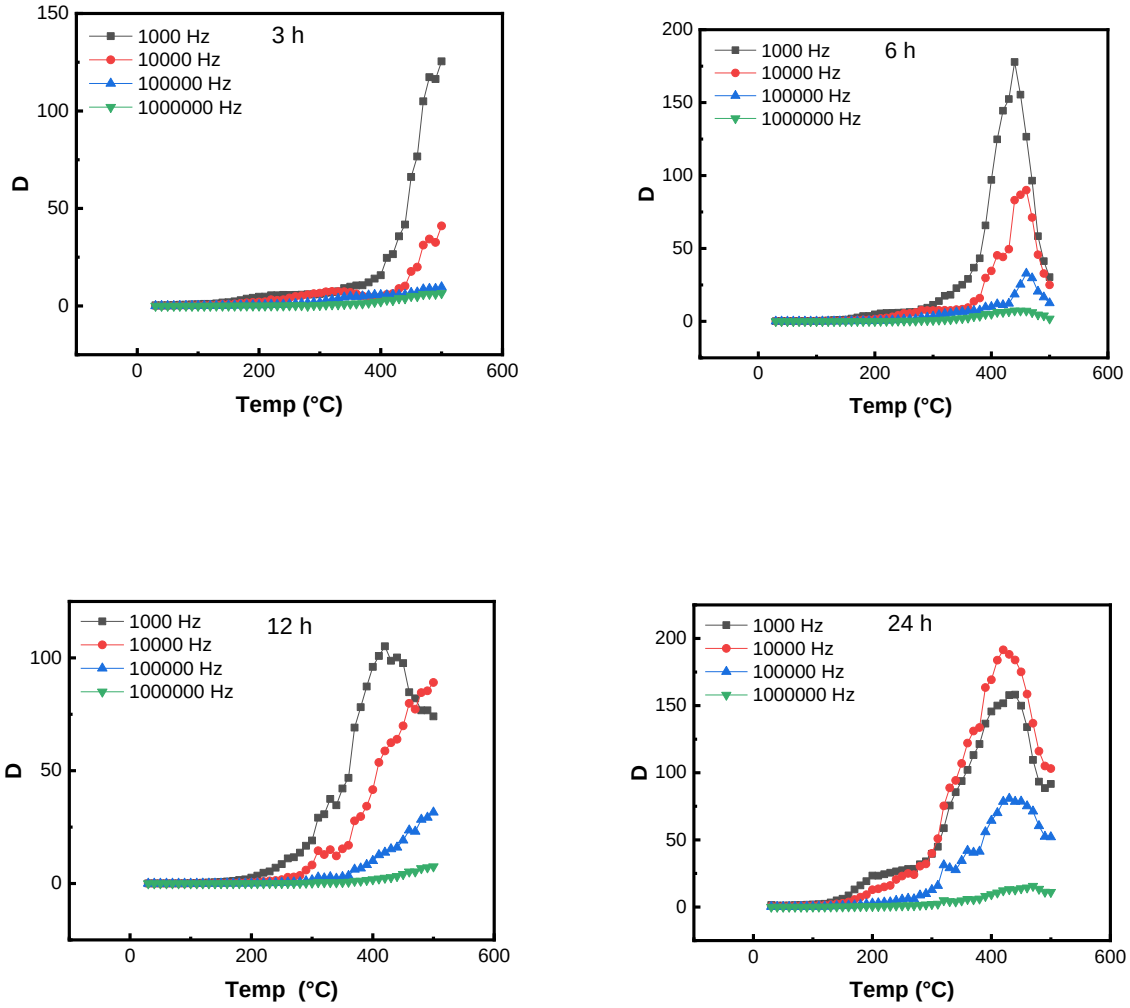

Figure 4.13: Temperature dependence of dielectric loss at different frequencies for LGP sample sintered at 3 h, 6 h, 12 h, and 24 h.

4.4 CONDUCTIVITY

A prominent factor that reveals reliable information about the transport phenomenon in materials is AC electrical conductivity. Moreover, AC measurements are also helpful in identifying the nature of this conduction mechanism [45].

From Figure 4.14, AC conductivity increases linearly with an increase in frequency. This behavior is a feature of hopping type mechanism for electric conduction [69]. To further investigate this, we look at the activation energies at different frequencies.

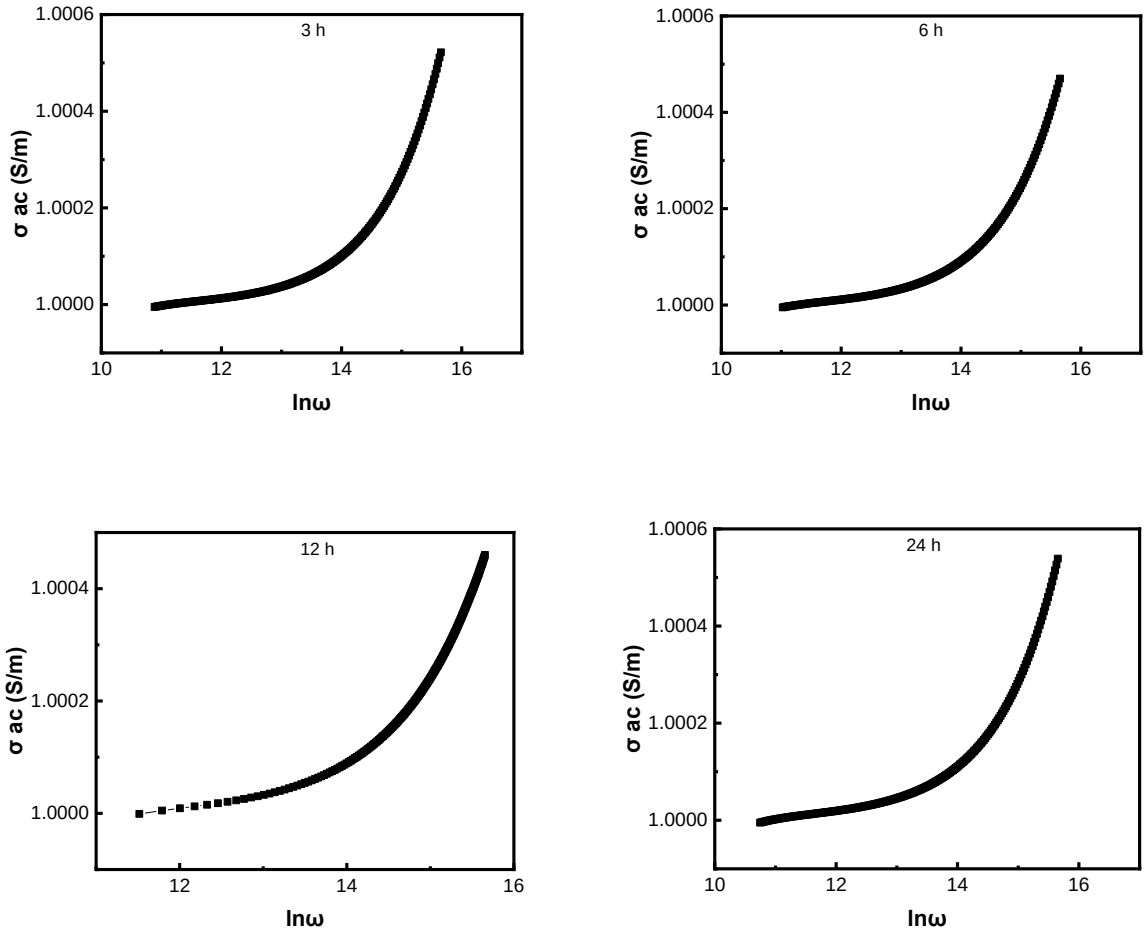

Figure 4.14: Frequency dependence on conductivity for LGP sample sintered at 3 h, 6 h, 12 h, and 24 h.

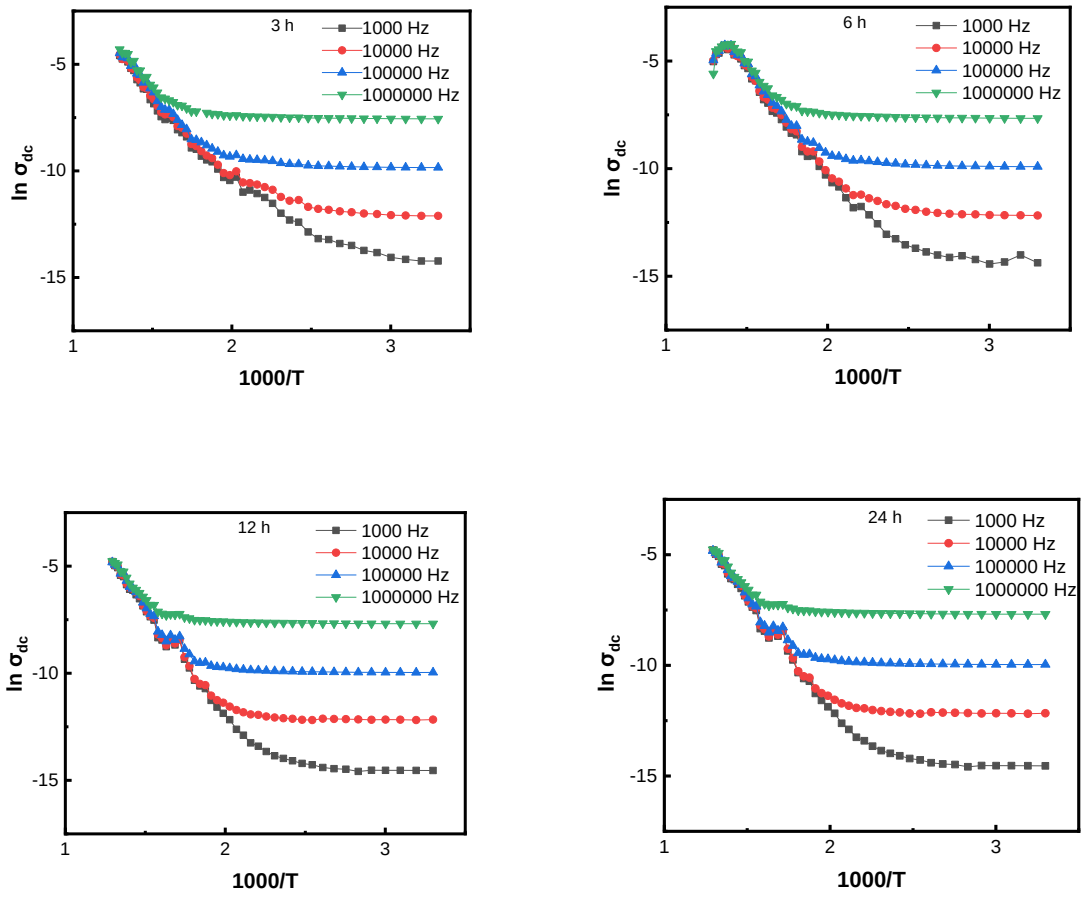

Figure 4.15: DC conductivity dependence on the inverse of absolute temperature at different frequencies for LGP sample sintered at 3 h, 6 h, 12 h, and 24 h.

The DC conductivity's dependence on the temperature at 1 kHz, 10 kHz, 100 kHz, and 1 MHz is plotted for all the samples of LGP. We can see that DC conductivity increases with an increase in temperature from Figure 4.15, and thus it shows that LGP's charge transportation properties are thermally activated. To get a better understanding, we look at the activation energy (E_a), which is calculated using the Arrhenius equation [70].

$$\sigma_{ac} = \sigma_0 e^{\frac{-E_a}{kT}} \tag{11}$$

where k is Boltzmann constant (= 0.00008617 eV/K).

Table 4.5: Activation energy of LGP samples

LGP Sample	Activation energy at 1 kHz	Activation energy at 10 kHz	Activation energy at 100 kHz	Activation energy at 1 MHz
800 °C, 3 h	0.83214 eV	0.78646 eV	0.76445 eV	0.61621 eV
800 °C, 6 h	0.71100 eV	0.67822 eV	0.62964 eV	0.51687 eV
800 °C, 12 h	0.87707 eV	0.86699 eV	0.83591 eV	0.57126 eV
800 °C, 24 h	0.47463 eV	0.45587 eV	0.45182 eV	0.43487 eV

The sample sintered for 24 h has the lowest activation energy compared to the rest. Furthermore, the values indicate that the increase in frequency decreases the activation energy of the LGP sample. It could be attributed to the fact that electronic jump between localized states is improved by the applied field frequency, which results in increased conductivity.

4.5 Structure and Morphology of LGP Thin Films

The XRD data of LGP films are shown in Figure 4.16. The substrates used for the deposition of thin films was silicon (100) wafers. Before deposition, the wafers were sonicated to ensure their cleanness. The XRD of thin films indicated amorphous nature for deposition temperatures under 500 °C. However, above 500 °C substrate temperature, the samples are polycrystalline. The 700 °C substrate temperature sample accurately matches the LGP XRD from the literature.

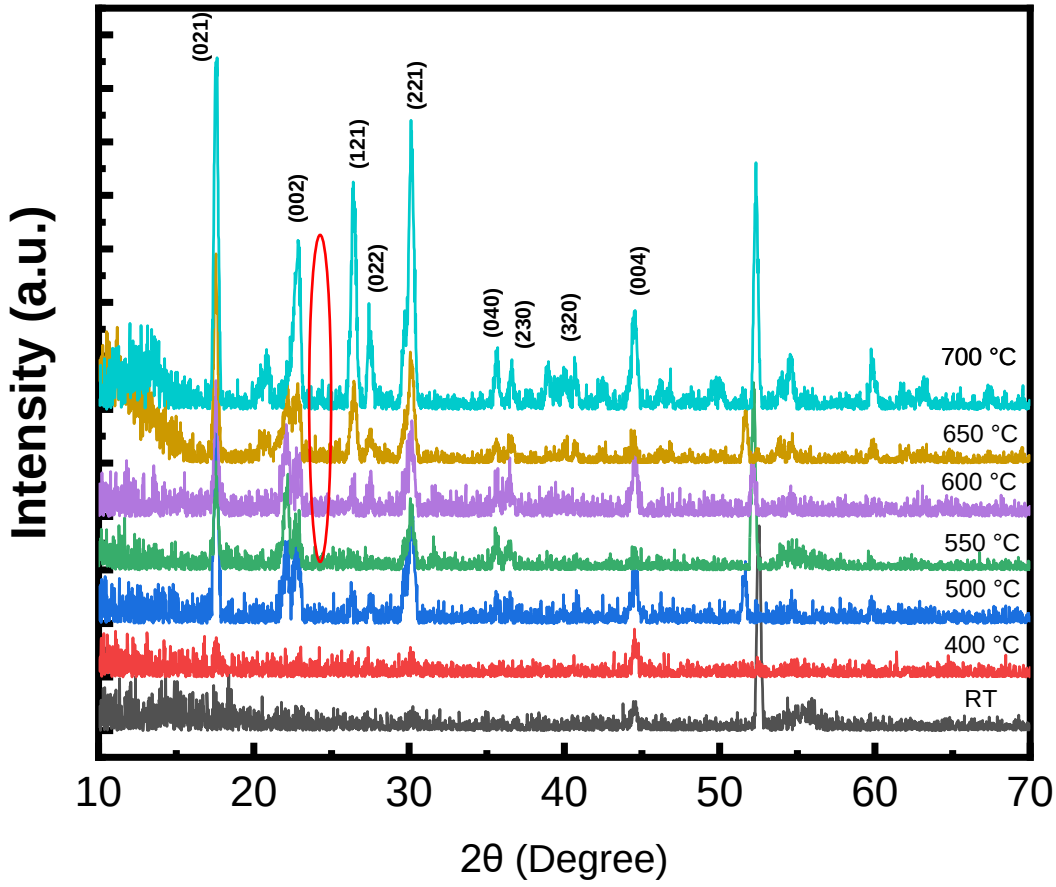

Figure 4.16: XRD of a thin film for varying substrate pressure.

The difference between 500 °C, 550 °C, 600 °C, 650 °C and 700 °C substrate temperature samples is the relative intensity of peak at 20.75°. This peak is highlighted with a red oval in Figure 4.16. The relative intensity is nonexistent or close to zero at 500 °C and slowly begins to increase as the substrate temperature increases. Thus, increasing substrate temperature increases the crystallinity of the sample. From XRD, the crystallite sizes were estimated using Scherrer's equation. The variation in the crystallite size of LGP films is as presented in Table 4.6.

Table 4.6: Crystallite size of LGP thin films

LGP Sample	The crystallite size (nm)
500 °C	22.0763023
550 °C	21.34222454
600 °C	22.5946647
650 °C	19.9558645
700 °C	21.62465361

There is little variation of the crystallite sizes except for 650 °C. This could be the result of the unusual XRD measurement observed below the 2θ of 14°. There were no similarities in literature and hence is more likely an artifact.

The SEM data of LGP films are shown in Figures 4.17 to 4.29. From the SEM images, it is evident that there is a lack of grain growth, indicating the amorphous nature of thin film on the substrate. This agrees with XRD of sample deposited on the substrate at RT. The XRD pattern of the thin film where LGP was deposited on the substrate from 500 °C indicated crystallinity. From the corresponding SEM images, grain growth is visible as seen in Figure 4.18. The grain growth is most prominent in the SEM images of the 700 °C (Figure 4.19) polycrystalline sample. Based on the SEM images, the mean grain size was measured to be around 250 nm to 500 nm.

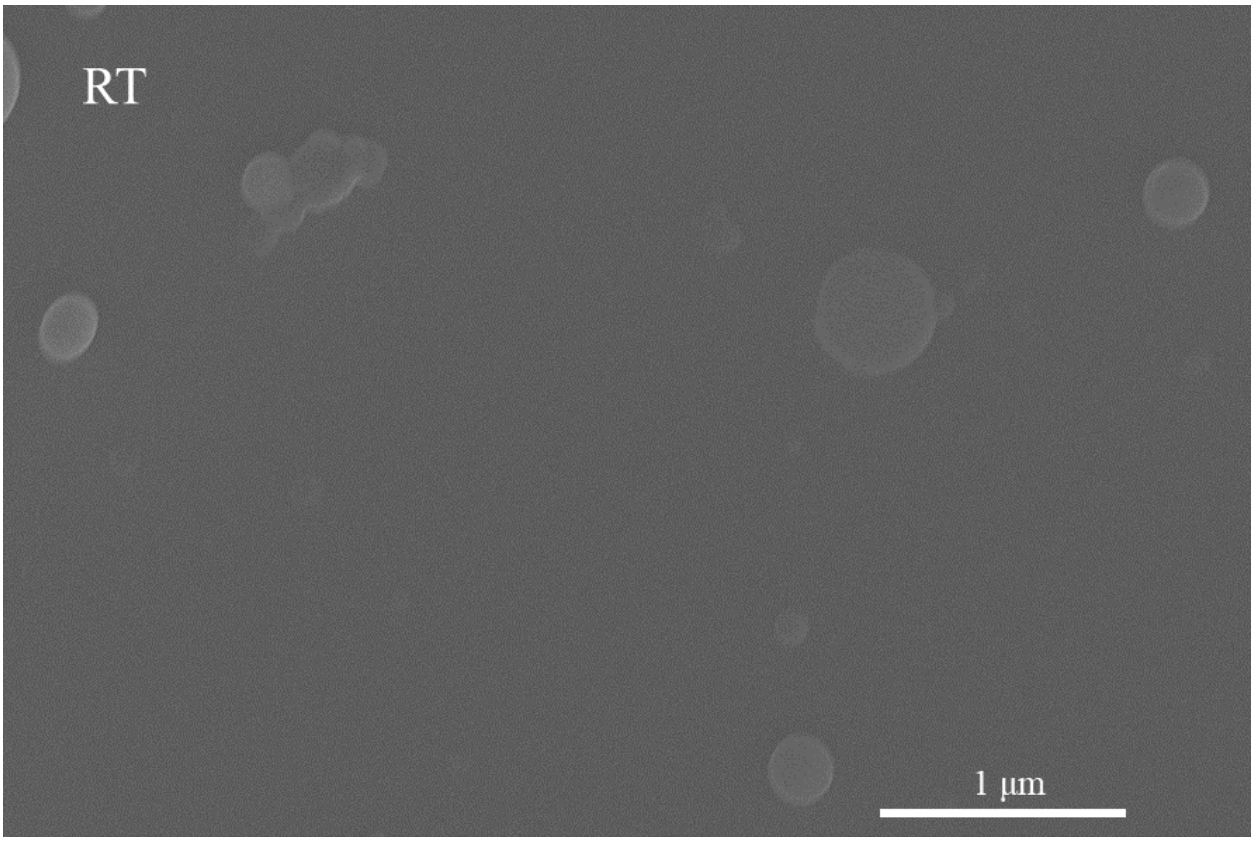

Figure 4.17: SEM images of thin film deposited at RT

.

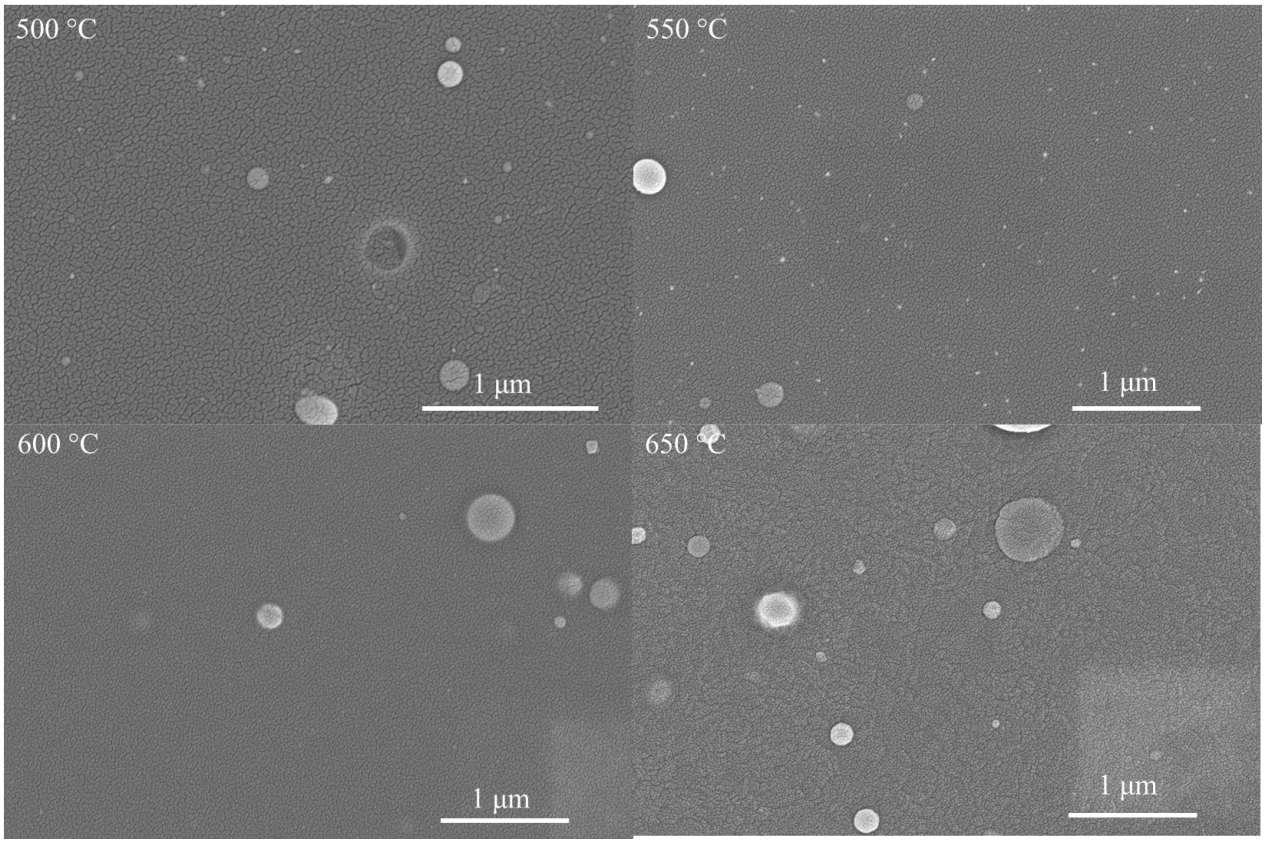

Figure 4.18: SEM images of thin film deposited at 500 °C to 650 °C.

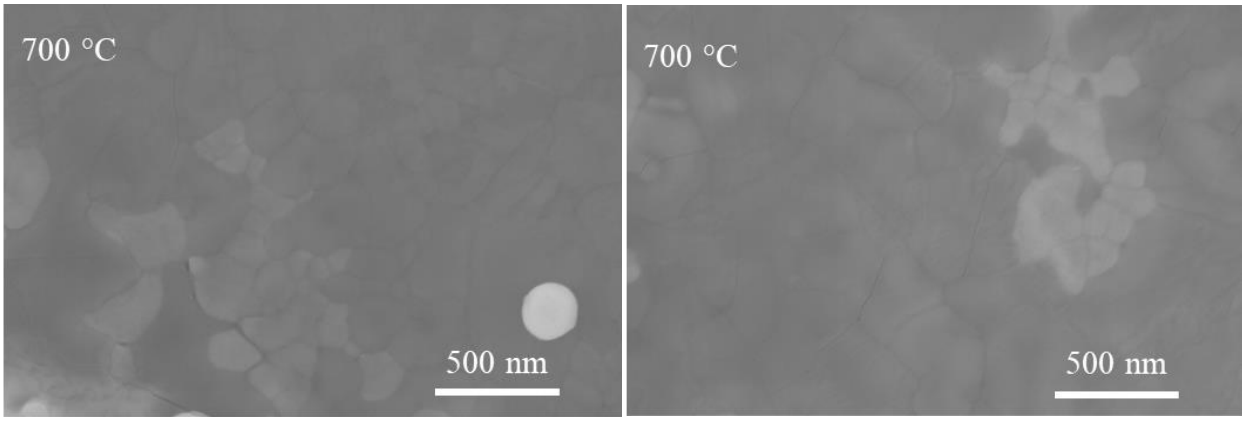

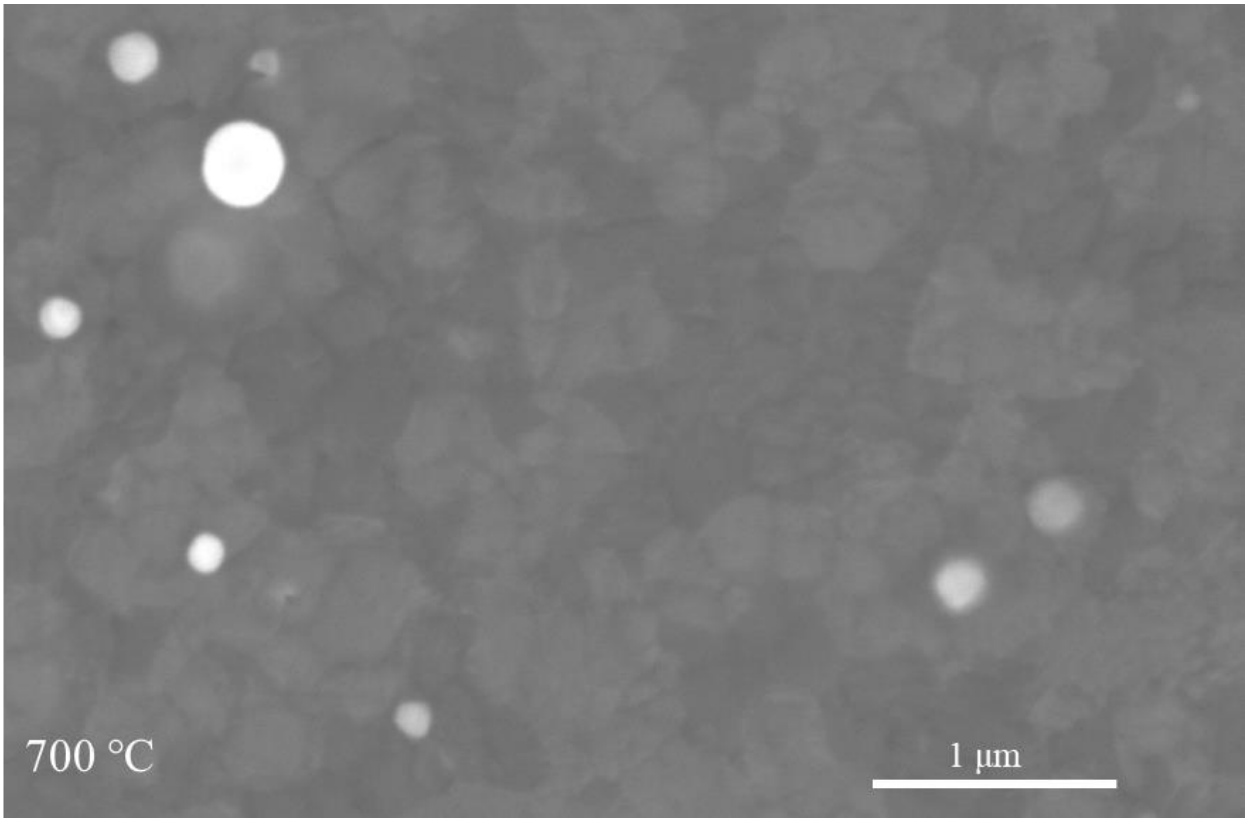

Figure 4.19: SEM images of thin film deposited at 700 °C.

4.6 SPECTROSCOPIC ELLIPSOMETRY

The optical quantities measured are ellipsometry angles Psi (Ψ) and Delta (Δ). They are related to the optical and structural properties of the sample as Δ is the difference in phase shift and Ψ is the component of amplitude ratio. They are defined as

$$\Delta = \delta_p - \delta_s \tag{12}$$

$$\tan \Psi = \frac{|r_p|}{|r_s|} \tag{13}$$

$$\rho = \frac{r_p}{r_s} = \tan \Psi \, e^{-i\Delta} \tag{14}$$

where the complex Fresnel's reflection coefficients for light polarized perpendicular and parallel to the plane of incidence is denoted by rho (ρ).

The spectral dependencies of Ψ and Δ can be utilized with relevant models to determine film thickness as well as the refractive index (n) and extinction coefficients (k).[54] The values would be determined based on the best fit between the simulated and measured spectra. Mean-squared error (MSE) would be minimized by utilizing the fitting of the Levenberg-Marquardt regression algorithm.

$$\mathrm{MSE} = \frac{1}{2N-M}\sum_{i=1}^{n}\left[\left\{\frac{(\Psi_{exp}-\Psi_{calc})}{\sigma_{\Psi_i}^{exp}}\right\}^2 + \left\{\frac{(\Delta_{exp}-\Delta_{calc})}{\sigma_{\Delta_i}^{exp}}\right\}^2\right] \quad (15)$$

where Ψ_{exp}, Ψ_{calc}, Δ_{exp}, and Δ_{calc} represent the measured and calculated ellipsometry functions, while N indicates the number of Ψ, Δ pairs, M represents the number of fitted parameters in the model and σ accounts for standard deviations in the experimental data [71].

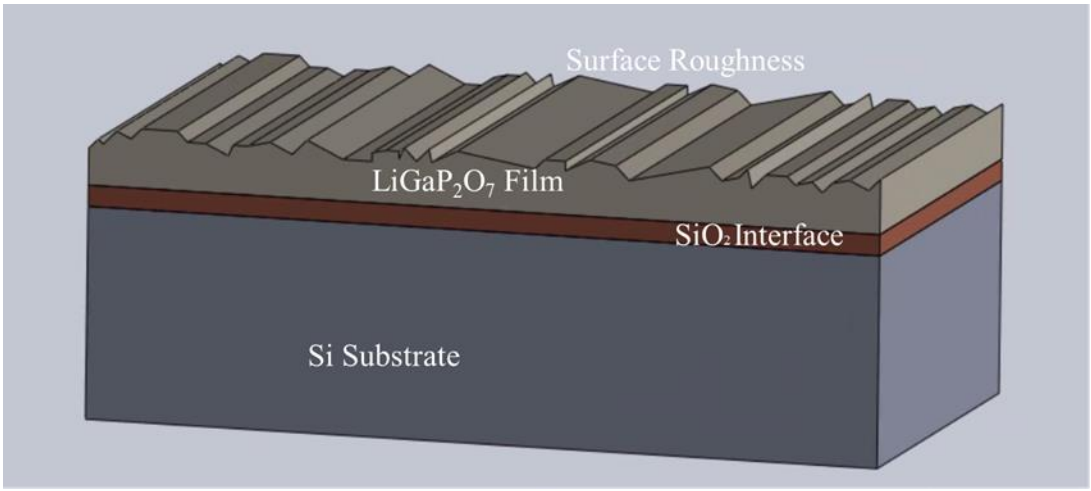

Figure 4.20: Optical model used for SE data analysis (by Nanthakishore Makeswaran, CMR, UTEP)

Deriving useful physical information from the ellipsometry measurements involves utilizing an optical model of the sample. The model should consider the multiple layers with their corresponding optical properties. Additionally, interfaces between layers act as optical boundaries

where light can be refracted or reflected as described by the Fresnel relations. The optical model we used us shown in Figure 4.20.

There is little published literature for LGP in terms of its optical properties to act as a guide. Hence, a variety of models were tested to fit the physical data and explain the optical properties of the thin films. Ultimately the Cauchy dispersion model (used for non-metallic materials such as dielectrics and semiconductors) yielded the best results. The Cauchy equation for n as a function of wavelength λ is as follows:

$$n(\lambda) = A + {}^{B}/_{\lambda^2} + {}^{C}/_{\lambda^4} \tag{16}$$

where A, B, and C stand for the Cauchy coefficients specific to the material with A being the constant that dominates n (λ) for long wavelengths, while B and C control curvature the most in the mid-visible spectrum and shorter wavelengths respectively.

The model can also be used to derive the k by:

$$k(\lambda) = d + {}^{e}/_{\lambda^2} + {}^{f}/_{\lambda^4} \tag{17}$$

where d, e, and f represent material specific constants [72].

The simulated values, as determined by the Cauchy dispersion model, showed close agreement to the experimental data, as can be seen in the curves for individual temperatures shown in the Appendix.

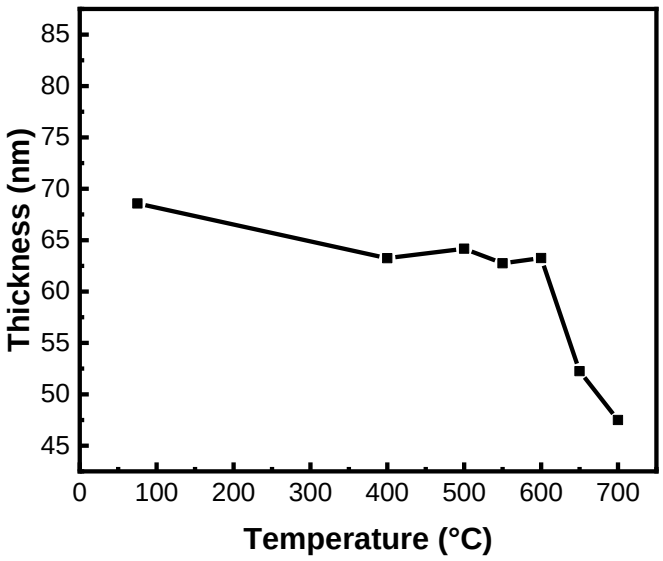

Figure 4.21: Variation of the thickness of the thin film

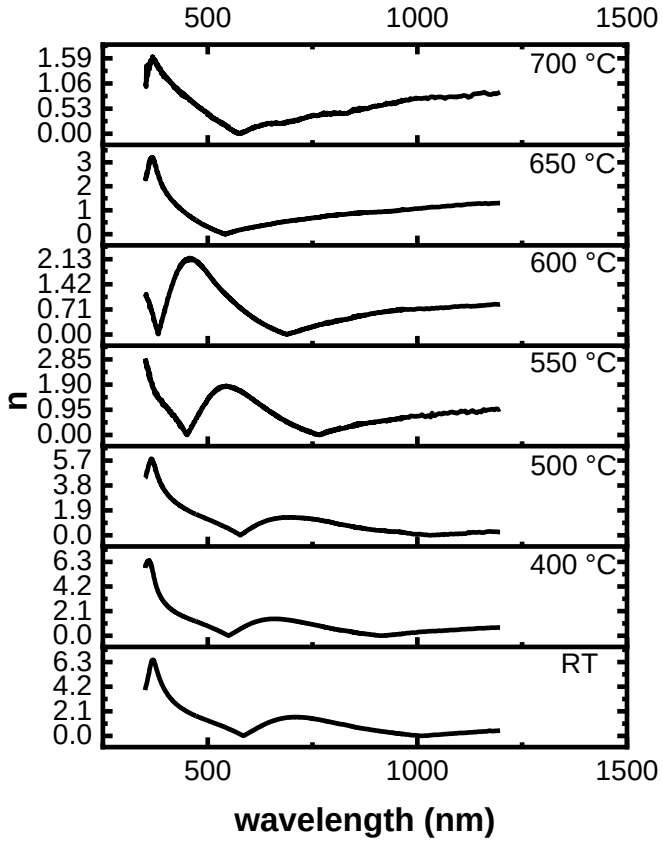

Figure 4.22: n values across deposition temperatures.

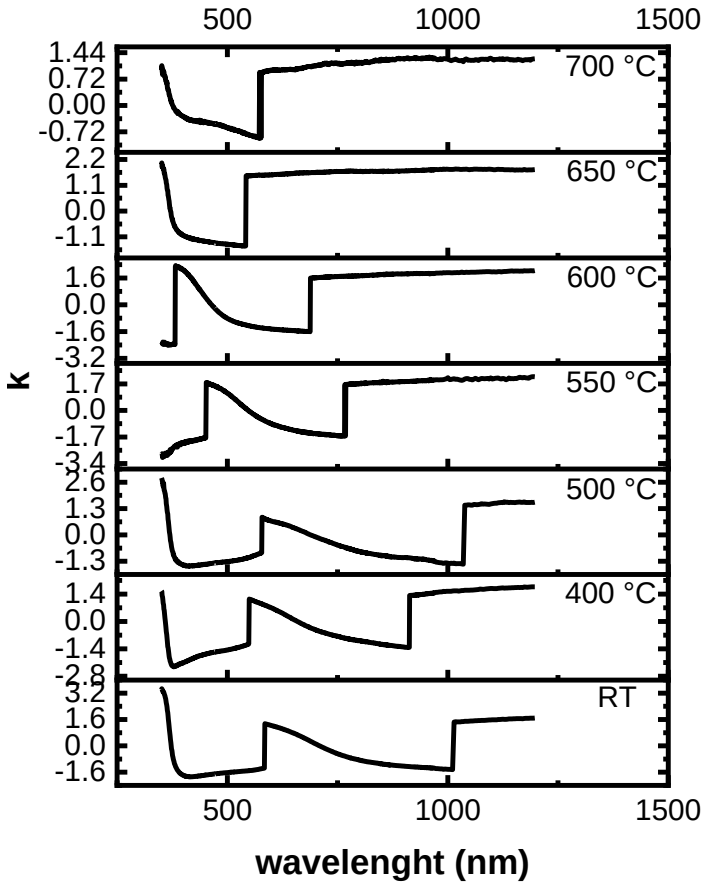

Figure 4.23: k values across deposition temperatures.

The SE analysis yielded the thickness of the samples utilizing the Cauchy dispersion model. The thickness of the sample decreases with an increase in substrate temperature and an increase in crystallinity, as indicated in figure 4.21. The dispersion profiles for the refractive index (n) can be seen in figure 4.22. Across all temperatures, there is an increase at shorter wavelengths, which corresponds to the fundamental absorption of energy across the bandgap. Moreover, it should be noted that there is a clear trend of decreasing absorption with higher temperatures.

On the other hand, the behavior of extinction coefficient (k) across the various samples is more erratic, as seen in Figure 4.23. At low to mid wavelengths, k values are generally at or close

to zero, indicating low optical losses due to absorption with sharp increases at higher and very low wavelengths caused with fundamental absorption across the bandgap. The most unexpected, however, was the presence of areas of negative k values. It indicates the possibility of luminescence triggered through excitation of specific wavelengths.

4.7 SECOND HARMONIC GENERATION (SHG)

The images obtained from the power scan helped in identifying the regions on the thin film with a strong SHG signal. The mean intensities (arbitrary units 0–255) of these regions were calculated and plotted against laser power (mW) on a logarithmic scale (Figure 4.24). A linear fit was used to obtain a slope of 1.46, 1.32, and 1.49 from the 700 °C, RT, and 500 °C samples, respectively.

From the polarization scans, a graph was plotted with mean intensities (arbitrary units) on the radial axis and light polarization (degrees) on the angular axis (Figure 4.25). These plots show distinct dipolar shape with some quadrupolar character. This indicates a clear dependence of SHG activity with the polarization of incident light.

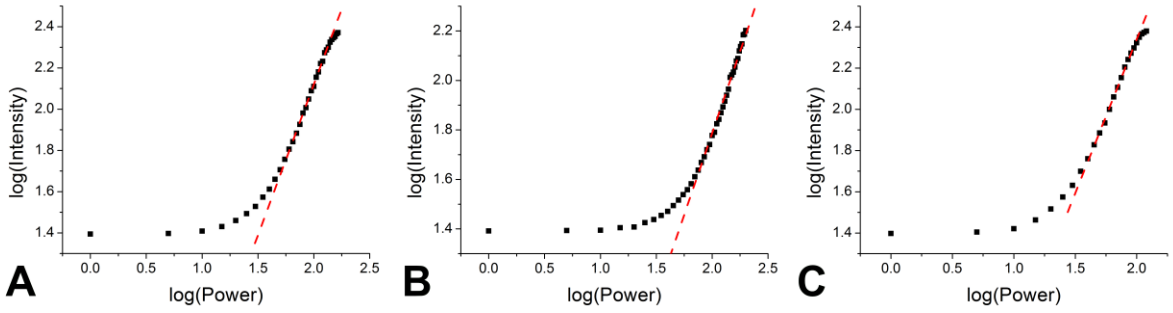

Figure 4.24: Log-log plots of SHG intensity vs. laser power in LGP samples A) 700°C, B) Room temperature and C) 500°C

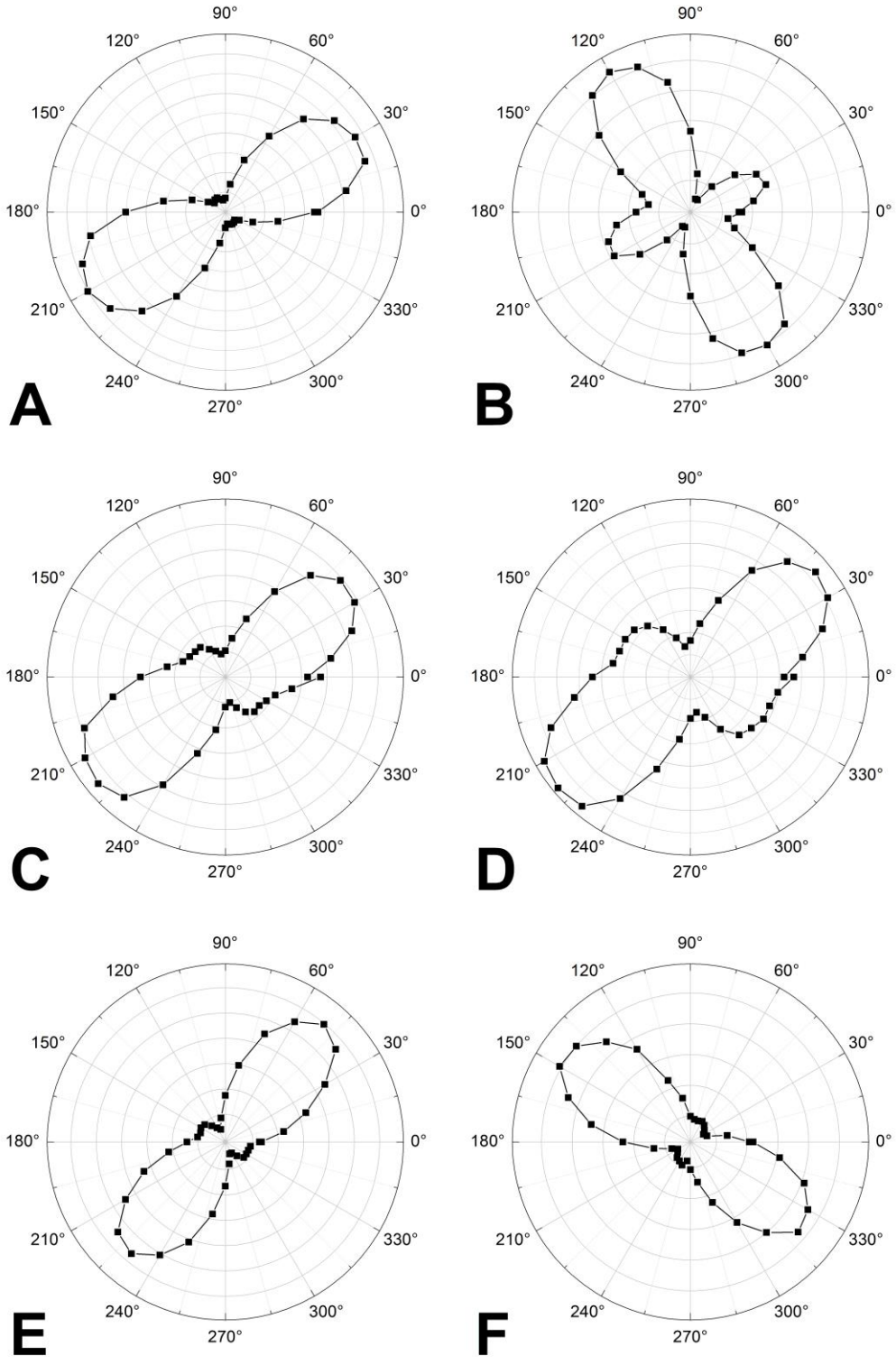

Figure 4.25: Polar plots of SHG intensity (radial axis) vs. polarization of incident laser (angular axis) in different regions of MOD-LGPO 700°C (A, B), room temperature (C, D), and 500°C (E, F)

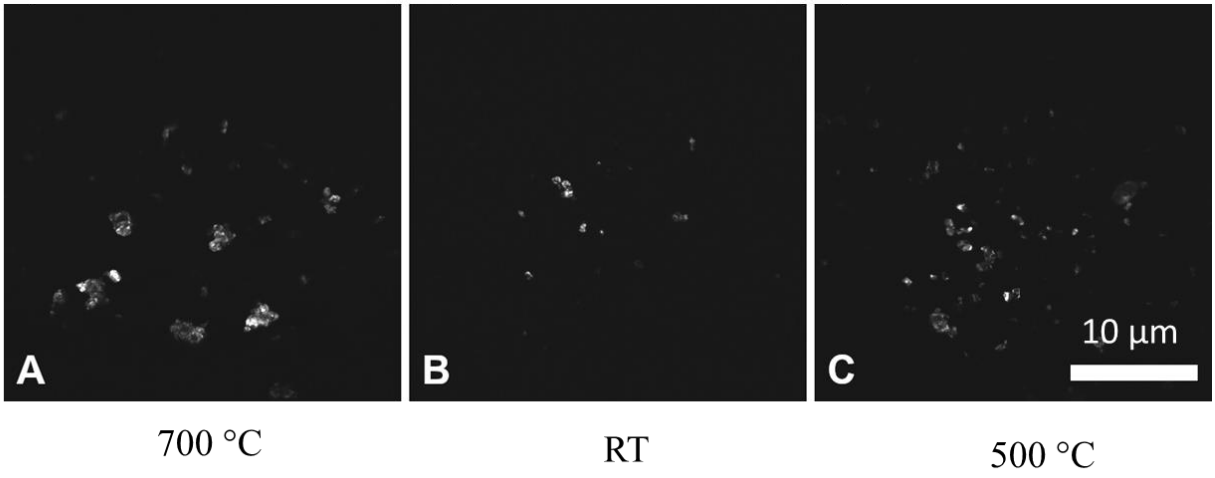

Figure 4.26: Micrographs of SHG activity (seen as white) in MOD-LGPO samples A) 700°C, B) Room temperature, and C) 500°C.

The micrographs extracted from the blue channel are shown in Figure 4.26, with the white representing SHG activity. The most interesting observation from these is the SHG signal in the RT sample, which is amorphous. This indicates the presence of nanocrystalline particles embedded in the amorphous matrix, corroborated by the single crystalline peaks present in the XRD.

Chapter 5: Conclusions and Future Work

5.1 Conclusions

$LiGaP_2O_7$, a novel material having monoclinic symmetry with $P2_1$ space group, was synthesized using a conventional solid-state, high-temperature chemical synthesis reaction. The phase purity of this material was obtained after calcinating at 650 °C for 8 h. The effect of sintering time (3 h, 6 h, 12 h, and 24 h) while keeping the temperature fixed at 800 °C indicated a trend. The XRD indicated a change in lattice parameters, and Rietveld refinement shows a trend of decreasing unit cell volume. The grain size measured using SEM images showed an increase with sintering time. From the SEM images, we also note a decrease in porosity with an increase in sintering time. Furthermore, refinement concluded that there was a decrease in unit cell volume with an increase in sintering time.

Impedance spectroscopy measurements were taken over a frequency range (1 kHz to 1 MHz) with increasing temperature (30 °C to 500 °C). The dielectric constant decreases with an increase in frequency. Moreover, dielectric constant increases with an increase in temperature after ~200 °C. The modified Debye's equation shows that the experimental and calculated values of dielectric constant are in good agreement and suggests the possibility that multiple ions contribute to the dielectric relaxation process. The conductivity of the sample increases with an increase in frequency, suggesting the hopping type conduction mechanism. Utilizing the Arrhenius equation, the activation energy calculated, which showed a decreasing trend with increasing frequency and sintering time.

The XRD of the PLD LGP thin films indicate amorphous nature for samples deposited at lower temperatures. The onset of crystallization was found at 500 °C. The XRD of 700 °C polycrystalline thin film was in good agreement with literature and utilizing SEM images, and we

estimate the size to be around 250 nm to 500 nm. The Cauchy dispersion model was used to obtain the optical parameters using SE. The thickness of the thin film's deceases with an increase in substrate temperatures and increasing crystallinity. Furthermore, the absorption was decreased with increasing substrate temperature. The excitation coefficient measurement suggested the possibility of luminescence under a specific wavelength. SHG imagining shows dependence on intensity to the polarization of the incident beam. The presence of SHG activity indicates nanocrystalline present in the amorphous matrix.

This study explores the novel optical and electronic materials for utilization under extreme environments. It also demonstrates the ability to engineer the Li-Ga based pyrophosphate's properties to meet application requirements.

5.2 FUTURE WORK

Based on the results of the present work, the following avenues can be taken for future research:

1) LGP ceramic showed promise for battery application.
2) The mechanism for thin film growth on other substrates is not explored.
3) Single crystal of LGP has shown good phase matching behavior, and thus, an application that requires frequency conversion should be explored.
4) The effect of annealing on microstructure has not been explored.
5) The electrical and mechanical properties of thin films could be explored.

Appendix

SE FITTING

Ψ measured and modeled

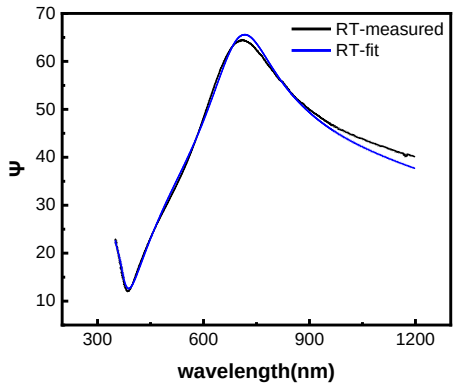

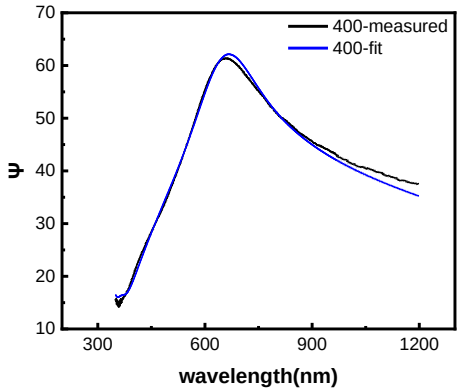

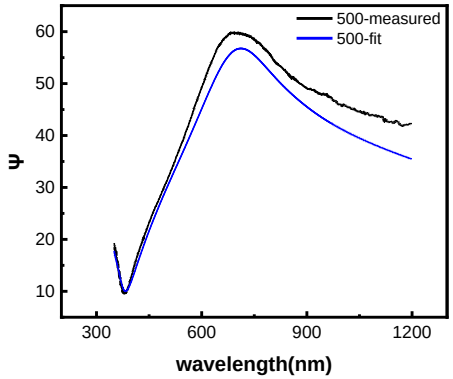

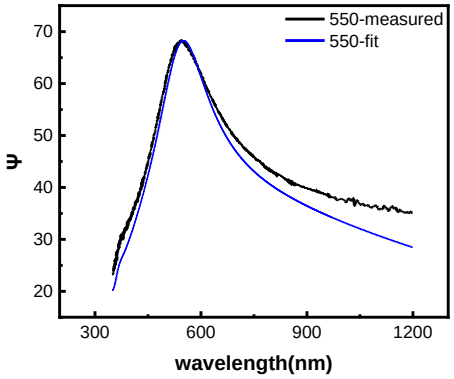

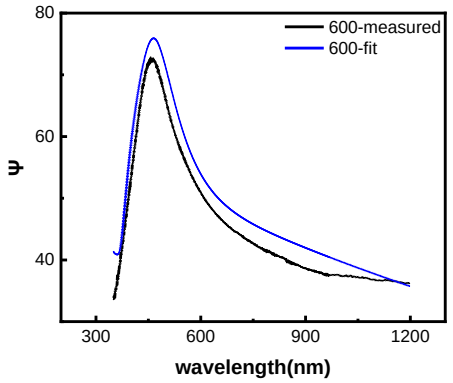

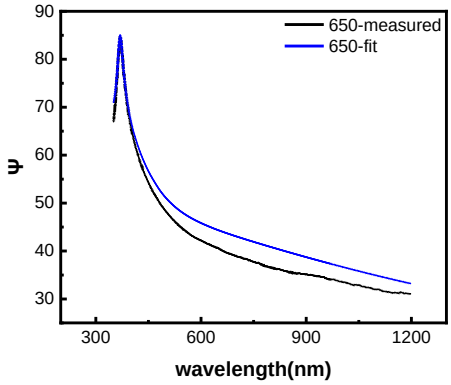

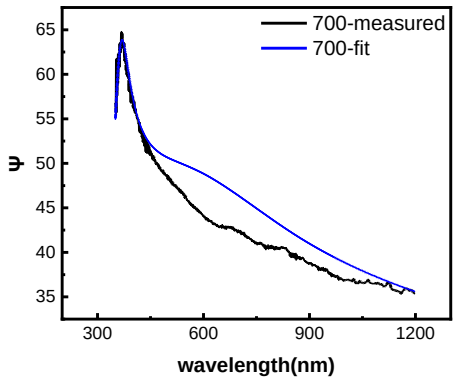

Δ measured and modeled

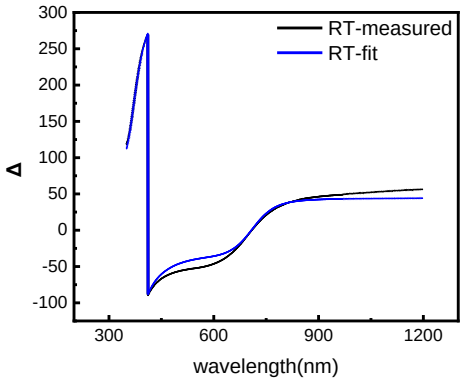

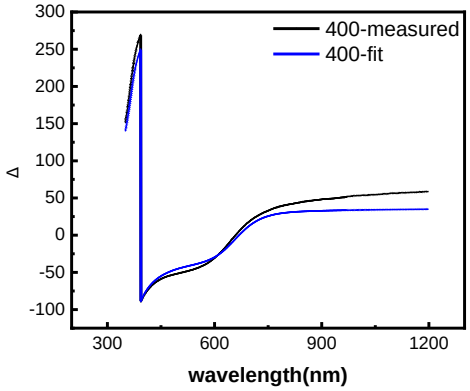

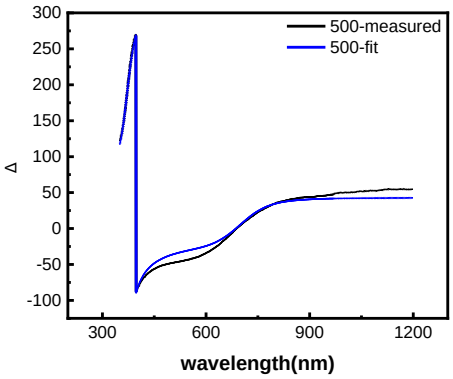
500-measured
500-fit
Δ
wavelength(nm)

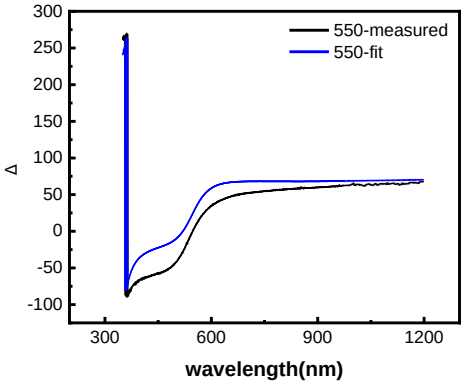
550-measured
550-fit
Δ
wavelength(nm)

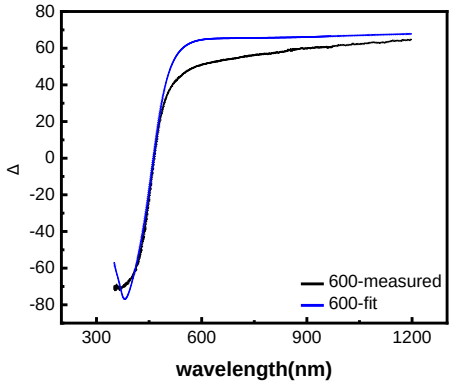
600-measured
600-fit
Δ
wavelength(nm)

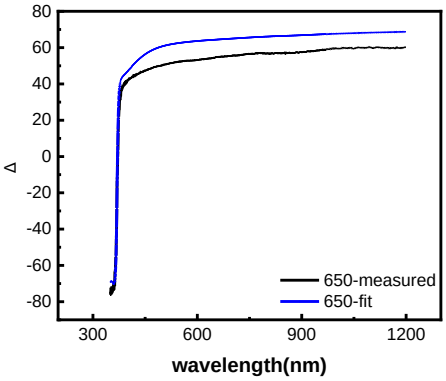
650-measured
650-fit
Δ
wavelength(nm)

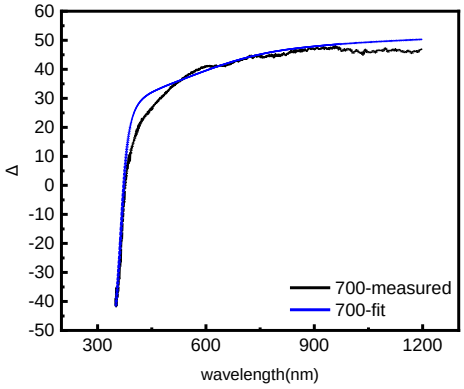
700-measured
700-fit
Δ
wavelength(nm)

References

[1] Y. Filinchuk, V. V. Lisnyak, D.A. Stratiichuk, N. V. Stus, Crystal structure of Nax(MoO)5(P2O7)4 studied by synchrotron X-ray diffraction, J. Alloys Compd. 463 (2008) 124–128. https://doi.org/10.1016/j.jallcom.2007.09.036.

[2] I.M. Nagpure, K.N. Shinde, V. Kumar, O.M. Ntwaeaborwa, S.J. Dhoble, H.C. Swart, Combustion synthesis and luminescence investigation of Na3Al2(PO4)3:RE (RE = Ce3+, Eu3+ and Mn2+) phosphor, J. Alloys Compd. 492 (2010) 384–388. https://doi.org/10.1016/j.jallcom.2009.11.110.

[3] R. Pang, C. Li, L. Jiang, Q. Su, Blue long lasting phosphorescence of Tm3+ in zinc pyrophosphate phosphor, J. Alloys Compd. 471 (2009) 364–367. https://doi.org/10.1016/j.jallcom.2008.03.104.

[4] R. Ternane, M. Ferid, Y. Guyot, M. Trabelsi-Ayadi, G. Boulon, Spectroscopic properties of Yb3+ in NaYbP2O7 diphosphate single crystals, J. Alloys Compd. 464 (2008) 327–331. https://doi.org/10.1016/j.jallcom.2007.09.104.

[5] Y. Ben Taher, A. Oueslati, K. Khirouni, M. Gargouri, Dielectric Spectroscopy and Modulus Study of Aluminum Diphosphate AgAlP2O7, J. Clust. Sci. 26 (2015) 1655–1669. https://doi.org/10.1007/s10876-015-0865-y.

[6] Y. Ben Taher, R. Hajji, A. Oueslati, M. Gargouri, Infra-red, NMR Spectroscopy and Transport Properties of Diphosphate NaAlP2O7, J. Clust. Sci. 26 (2015) 1279–1294. https://doi.org/10.1007/s10876-014-0812-3.

[7] K. SASAKI, N. OHNO, EXCITON LUMINESCENCE OF HYDROGEN-BONDED FERROELECTRIC PbHPO 4, Nonlinear Opt. 29 (2002) 615–620. https://doi.org/10.1080/1058726021000045289.

[8] T. Fuyuki, K. Sasaki, N. Ohno, Time-resolved photoluminescence of hydrogen-bonded ferroelectrics PbHPO4, in: J. Lumin., North-Holland, 2005: pp. 250–254. https://doi.org/10.1016/j.jlumin.2004.09.065.

[9] N. Eliaz, N. Metoki, Calcium phosphate bioceramics: A review of their history, structure, properties, coating technologies and biomedical applications, Materials (Basel). 10 (2017). https://doi.org/10.3390/ma10040334.

[10] P. Bhanja, J. Na, T. Jing, J. Lin, T. Wakihara, A. Bhaumik, Y. Yamauchi, Nanoarchitectured Metal Phosphates and Phosphonates: A New Material Horizon toward Emerging Applications, Chem. Mater. 31 (2019) 5343–5362. https://doi.org/10.1021/acs.chemmater.9b01742.

[11] X. Li, X. Xiao, Q. Li, J. Wei, H. Xue, H. Pang, Metal (M = Co{,} Ni) phosphate based materials for high-performance supercapacitors, Inorg. Chem. Front. 5 (2018) 11–28. https://doi.org/10.1039/C7QI00434F.

[12] D.J. Lockwood, N. Ohno, R.J. Nelmes, H. Arend, Dynamics and statics of the ferroelectric phase transition in {PbHPO}4, J. Phys. C Solid State Phys. 18 (1985) L559--L565. https://doi.org/10.1088/0022-3719/18/19/004.

[13] Y. Abe, Superprotonic Conductors of Glassy Zirconium Phosphates, J. Electrochem. Soc. 143 (1996) 144. https://doi.org/10.1149/1.1836399.

[14] T.E. Warner, W. Milius, J. Maier, New Copper Phosphates as Ionic or Mixed Conductors, Berichte Der Bunsengesellschaft Für Phys. Chemie. 96 (1992) 1607–1613. https://doi.org/10.1002/bbpc.19920961117.

[15] X. ZHANG, W. ZHENG, H. ZHANG, C. CHEN, J. SEO Hyo, Luminescence of Eu2+ and Eu2+-Mn2+ in sodium scandium diphosphate NaScP2O7 crystal, J. Rare Earths. 35

(2017) 453–459. https://doi.org/10.1016/S1002-0721(17)60933-5.

[16] M. Chaker, K. Horchani-Naifer, M. Férid, Structural and optical studies of KErP2O7diphosphate, J. Alloys Compd. 688 (2016) 104–110. https://doi.org/10.1016/j.jallcom.2016.07.047.

[17] A. Watras, P. Boutinaud, R. Pazik, P.J. Dereń, Luminescence - Structure relationships in MYP2O7:Eu3+ (M=K, Rb, Cs), J. Lumin. 175 (2016) 249–254. https://doi.org/10.1016/j.jlumin.2016.02.040.

[18] Y. Jiang, W. Liu, X. Cao, G. Su, L. Cao, R. Gao, A new type of KYP2O7 synthesized by the boric acid flux method and its luminescence properties, J. Alloys Compd. 657 (2016) 697–702. https://doi.org/10.1016/j.jallcom.2015.10.138.

[19] W. Hami, A. Zegzouti, M. Daoud, D. Zambon, M. Rossi, A. Vergara, F. Capitelli, A. Altomare, R. Rizzi, Synthesis, structural characterization and luminescent properties of Tb3+-doped AgLaP2O7 phosphors, Ceram. Int. 44 (2018) 19184–19190. https://doi.org/10.1016/j.ceramint.2018.06.271.

[20] R. Velchuri, B.V. Kumar, V.R. Devi, D.J. Prakash, M. Vithal, Solid-State Syntheses of Rare-Earth–Doped $Sr_{1-x}Ln_{2x/3}MgP_2O_7$ (Ln = Gd, Eu, Dy, Sm, Pr, and Nd; x = 0.05) by Metathesis Reactions and their Spectroscopic Characterization, Spectrosc. Lett. 44 (2011) 258–266. https://doi.org/10.1080/00387010.2010.515283.

[21] W. Hami, M. Daoud, D. Zambon, M. Elaatmani, A. Zegzouti, Synthesis and characterization of AgYP 2 O 7 pyrophosphate activated with Tb 3+ , Sm 3+ and Dy 3+ ions, Inorg. Chem. Commun. 102 (2019) 192–198. https://doi.org/10.1016/j.inoche.2019.02.013.

[22] D.E. HARRISON, H.A. McKINSTRY, F.A. HUMMEL, High-Temperature Zirconium

Phosphates, J. Am. Ceram. Soc. 37 (1954) 277–288. https://doi.org/10.1111/j.1151-2916.1954.tb14037.x.

[23] P. Krempl, G. Schleinzer, W. Wallnöfer, Gallium phosphate, gapo4: A new piezoelectric crystal material for high-temperature sensorics, Sensors Actuators, A Phys. 61 (1997) 361–363. https://doi.org/10.1016/S0924-4247(97)80289-0.

[24] R. Marom, S.F. Amalraj, N. Leifer, D. Jacob, D. Aurbach, A review of advanced and practical lithium battery materials, J. Mater. Chem. 21 (2011) 9938–9954. https://doi.org/10.1039/c0jm04225k.

[25] X.-B. Cheng, R. Zhang, C.-Z. Zhao, Q. Zhang, Toward Safe Lithium Metal Anode in Rechargeable Batteries: A Review, Chem. Rev. 117 (2017) 10403–10473. https://doi.org/10.1021/acs.chemrev.7b00115.

[26] Z. Liu, P.-G. Li, Y.-S. Zhi, X.-L. Wang, X.-L. Chu, W.-H. Tang, Review of gallium oxide based field-effect transistors and Schottky barrier diodes, Chinese Phys. B. 28 (2019) 17105. https://doi.org/10.1088/1674-1056/28/1/017105.

[27] S. Geller, Crystal structure of beta;-Ga2O3, J. Chem. Phys. 33 (1960) 676–684. https://doi.org/10.1063/1.1731237.

[28] Z. Wu, L. Jiao, X. Wang, D. Guo, W. Li, L. Li, F. Huang, W. Tang, A self-powered deep-ultraviolet photodetector based on an epitaxial Ga2O3/Ga:ZnO heterojunction, J. Mater. Chem. C. 5 (2017) 8688–8693. https://doi.org/10.1039/C7TC01741C.

[29] Q. Feng, L. Huang, G. Han, F. Li, X. Li, L. Fang, X. Xing, J. Zhang, W. Mu, Z. Jia, D. Guo, W. Tang, X. Tao, Y. Hao, Comparison Study of $β$ -Ga2O3 Photodetectors on Bulk Substrate and Sapphire, IEEE Trans. Electron Devices. 63 (2016) 3578–3583. https://doi.org/10.1109/TED.2016.2592984.

[30] K. Matsuzaki, H. Hiramatsu, K. Nomura, H. Yanagi, T. Kamiya, M. Hirano, H. Hosono, Growth, structure and carrier transport properties of Ga2O 3 epitaxial film examined for transparent field-effect transistor, in: Thin Solid Films, Elsevier, 2006: pp. 37–41. https://doi.org/10.1016/j.tsf.2005.08.187.

[31] Q. He, W. Mu, H. Dong, S. Long, Z. Jia, H. Lv, Q. Liu, M. Tang, X. Tao, M. Liu, Schottky barrier diode based on β-Ga2O3 (100) single crystal substrate and its temperature-dependent electrical characteristics, Appl. Phys. Lett. 110 (2017) 093503. https://doi.org/10.1063/1.4977766.

[32] C. V. Ramana, A. Mauger, F. Gendron, C.M. Julien, K. Zaghib, Study of the Li-insertion/extraction process in LiFePO4/FePO4, J. Power Sources. 187 (2009) 555–564. https://doi.org/10.1016/j.jpowsour.2008.11.042.

[33] C. V Ramana, A. Ait-Salah, S. Utsunomiya, A. Mauger, F. Gendron, C.M. Julien, Novel Lithium Iron Pyrophosphate (LiFe1.5P2O7) as a Positive Electrode for Li-Ion Batteries, Chem. Mater. 19 (2007) 5319–5324. https://doi.org/10.1021/cm071526m.

[34] V. Mani, N. Kalaiselvi, LiVP2O7/C: A New Insertion Anode Material for High-Rate Lithium-Ion Battery Applications, Inorg. Chem. 55 (2016) 3807–3814. https://doi.org/10.1021/acs.inorgchem.5b02795.

[35] Ģ. Vītiņš, Z. Kaņepe, A. Vītiņš, J. Ronis, A. Dindūne, A. Lūsis, Structural and conductivity studies in LiFeP2O7, LiScP2O7, and NaScP2O7, J. Solid State Electrochem. 4 (2000) 146–152. https://doi.org/10.1007/s100080050012.

[36] J. Barker, M.Y. Saidi, J.L. Swoyer, Electrochemical Insertion Properties of the Novel Lithium Vanadium Fluorophosphate, LiVPO[sub 4]F, J. Electrochem. Soc. 150 (2003) A1394. https://doi.org/10.1149/1.1609998.

[37] Y. Li, F. Liang, H. Song, W. Liu, Z. Lin, G. Zhang, Y. Wu, LiGaP 2 O 7 : A Potential UV Nonlinear-Optical Crystal, Inorg. Chem. 58 (2019) 6597–6600. https://doi.org/10.1021/acs.inorgchem.9b00970.

[38] B.L. Ellis, W.R.M. Makahnouk, Y. Makimura, K. Toghill, L.F. Nazar, A multifunctional 3.5V iron-based phosphate cathode for rechargeable batteries, Nat. Mater. 6 (2007) 749–753. https://doi.org/10.1038/nmat2007.

[39] A. Manthiram, J.B. Goodenough, Lithium insertion into Fe2(MO4)3 frameworks: Comparison of M = W with M = Mo, J. Solid State Chem. 71 (1987) 349–360. https://doi.org/10.1016/0022-4596(87)90242-8.

[40] J.B. Goodenough, H.Y.P. Hong, J.A. Kafalas, Fast Na+-ion transport in skeleton structures, Mater. Res. Bull. 11 (1976) 203–220. https://doi.org/10.1016/0025-5408(76)90077-5.

[41] A.K. Ivanov-Shits, Ionic conductivity of isostructural crystals of the superionic conductors Li3Fe2(PO4)4 and Li3Sc2(PO4)3, Phys. Solid State. 39 (1997) 72–74. https://doi.org/10.1134/1.1129834.

[42] A.K. Padhi, Phospho-olivines as Positive-Electrode Materials for Rechargeable Lithium Batteries, J. Electrochem. Soc. 144 (1997) 1188. https://doi.org/10.1149/1.1837571.

[43] A.A. Salah, P. Jozwiak, J. Garbaczyk, F. Gendron, A. Mauger, C.M. Julien, FTIR Features Of Lithium Iron Phosphates Used As Positive Electrodes In Rechargeable Lithium Batteries, IOP Publishing, 2006. https://doi.org/10.1149/MA2005-01/35/1385.

[44] M. Sassi, A. Bettaibi, A. Oueslati, K. Khirouni, M. Gargouri, Electrical conduction mechanism and transport properties of LiCrP2O7 compound, J. Alloys Compd. 649 (2015) 642–648. https://doi.org/10.1016/j.jallcom.2015.07.148.

[45] S. Nasri, M. Megdiche, M. Gargouri, DC conductivity and study of AC electrical conduction mechanisms by non-overlapping small polaron tunneling model in LiFeP2O7 ceramic, Ceram. Int. 42 (2016) 943–951. https://doi.org/10.1016/j.ceramint.2015.09.023.

[46] D. Li, ed., Non-Centrosymmetric, in: Encycl. Microfluid. Nanofluidics, Springer US, Boston, MA, 2008: p. 1457. https://doi.org/10.1007/978-0-387-48998-8_1113.

[47] S.-J. Cho, M.-J. Uddin, P. Alaboina, Chapter Three - Review of Nanotechnology for Cathode Materials in Batteries, in: L.M. Rodriguez-Martinez, N. Omar (Eds.), Emerg. Nanotechnologies Recharg. Energy Storage Syst., Elsevier, Boston, 2017: pp. 83–129. https://doi.org/https://doi.org/10.1016/B978-0-323-42977-1.00003-0.

[48] H.-U. Krebs, M. Weisheit, J. Faupel, E. Süske, T. Scharf, C. Fuhse, M. Störmer, K. Sturm, M. Seibt, H. Kijewski, D. Nelke, E. Panchenko, M. Buback, Pulsed Laser Deposition (PLD) -- A Versatile Thin Film Technique, in: B. Kramer (Ed.), Adv. Solid State Phys., Springer Berlin Heidelberg, Berlin, Heidelberg, 2003: pp. 505–518. https://doi.org/10.1007/978-3-540-44838-9_36.

[49] J.F. Ready, Chapter 3 - Practical Lasers, in: J.F. Ready (Ed.), Ind. Appl. Lasers (Second Ed., Second Edi, Academic Press, San Diego, 1997: pp. 66–130. https://doi.org/https://doi.org/10.1016/B978-012583961-7/50005-3.

[50] B. Fultz, J. Howe, Diffraction and the X-Ray Powder Diffractometer, in: 2013: pp. 1–57. https://doi.org/10.1007/978-3-642-29761-8_1.

[51] J. Goldstein, D. Newbury, J. Michael, N. Ritchie, Scanning electron microscopy and X-ray microanalysis, 2017. https://books.google.com/books?hl=en&lr=&id=D0I_DwAAQBAJ&oi=fnd&pg=PR5&ots=35TJ4sDkuh&sig=g5x2v-aRrGkMAKl38onHrsPSyv4 (accessed July 22, 2020).

[52] Q.H. Lu, F. Zheng, Polyimides for electronic applications, in: Adv. Polyim. Mater. Synth. Charact. Appl., Elsevier, 2018: pp. 195–255. https://doi.org/10.1016/B978-0-12-812640-0.00005-6.

[53] LCR METER IM3536 - Hioki, (n.d.). https://www.hioki.com/en/products/detail/?product_key=5824 (accessed July 22, 2020).

[54] E. Garcia-Caurel, A. De Martino, J.-P. Gaston, L. Yan, Application of Spectroscopic Ellipsometry and Mueller Ellipsometry to Optical Characterization, Appl. Spectrosc. 67 (2013) 1–21. http://as.osa.org/abstract.cfm?URI=as-67-1-1.

[55] P. Bianchini, A. Diaspro, Second Harmonic Generation Microscopy (SHG), in: Encycl. Biophys., Springer Berlin Heidelberg, 2013: pp. 2280–2283. https://doi.org/10.1007/978-3-642-16712-6_838.

[56] A.C. Aguilar, C.A. Diaz-Moreno, A.D. Price, R.K. Goutam, C.E. Botez, Y. Lin, R.B. Wicker, C. Li, Non-destructive optical second harmonic generation imaging of 3D printed aluminum nitride ceramics, Ceram. Int. 45 (2019) 18871–18875. https://doi.org/10.1016/j.ceramint.2019.06.121.

[57] A.D. Price, A.C. Aguilar, C.E. Botez, C. Li, Optical second harmonic generation imaging and x-ray diffraction of Cs 1 − x Rb x H 2 PO 4 proton conductor series , J. Appl. Phys. 127 (2020) 193105. https://doi.org/10.1063/5.0006922.

[58] Y. Acosta, Q. Zhang, A. Rahaman, H. Ouellet, C. Xiao, J. Sun, C. Li, Imaging cytosolic translocation of Mycobacteria with two-photon fluorescence resonance energy transfer microscopy, Biomed. Opt. Express. 5 (2014) 3990–4001. https://doi.org/10.1364/BOE.5.003990.

[59] R. Zsigmondy, P. Scherrer, Bestimmung der inneren Struktur und der Größe von

Kolloidteilchen mittels Röntgenstrahlen, in: Kolloidchem. Ein Lehrb., Springer Berlin Heidelberg, 1912: pp. 387–409. https://doi.org/10.1007/978-3-662-33915-2_7.

[60] J. Smit, W.H.P. J, Ferrites, Philips Technical Library, Eindhoven, The netherkands, 1959.

[61] S.G. Kakade, Y.R. Ma, R.S. Devan, Y.D. Kolekar, C. V. Ramana, Dielectric, Complex Impedance, and Electrical Transport Properties of Erbium (Er3+) Ion-Substituted Nanocrystalline, Cobalt-Rich Ferrite (Co1.1Fe1.9-xErxO4), J. Phys. Chem. C. 120 (2016) 5682–5693. https://doi.org/10.1021/acs.jpcc.5b11188.

[62] E.V. Gopalan, K.A. Malini, S. Saravanan, D.S. Kumar, Y. Yoshida, M.R. Anantharaman, Evidence for polaron conduction in nanostructured manganese ferrite, J. Phys. D. Appl. Phys. 41 (2008) 185005. https://doi.org/10.1088/0022-3727/41/18/185005.

[63] K.W. Wagner, Zur Theorie der unvollkommenen Dielektrika, Ann. Phys. 345 (1913) 817–855. https://doi.org/10.1002/andp.19133450502.

[64] C.G. Koops, On the dispersion of resistivity and dielectric constant of some semiconductors at audiofrequencies, Phys. Rev. 83 (1951) 121–124. https://doi.org/10.1103/PhysRev.83.121.

[65] P.A. Miles, W.B. Westphal, A. Von Hippel, Dielectric spectroscopy of ferromagnetic semiconductors, Rev. Mod. Phys. 29 (1957) 279–307. https://doi.org/10.1103/RevModPhys.29.279.

[66] M.T. Rahman, M. Vargas, C. V. Ramana, Structural characteristics, electrical conduction and dielectric properties of gadolinium substituted cobalt ferrite, J. Alloys Compd. 617 (2014) 547–562. https://doi.org/10.1016/j.jallcom.2014.07.182.

[67] K.S. Cole, R.H. Cole, Dispersion and absorption in dielectrics I. Alternating current characteristics, J. Chem. Phys. 9 (1941) 341–351. https://doi.org/10.1063/1.1750906.

[68] J. Anderson, Dielectrics, (1964). https://cds.cern.ch/record/105770 (accessed June 26, 2020).

[69] A.K. Jonscher, The “universal” dielectric response, Nature. 267 (1977) 673–679. https://doi.org/10.1038/267673a0.

[70] A.S.A. Khiar, R. Puteh, A.K. Arof, Conductivity studies of a chitosan-based polymer electrolyte, Phys. B Condens. Matter. 373 (2006) 23–27. https://doi.org/10.1016/j.physb.2005.10.104.

[71] C.M. Herzinger, P.G. Snyder, B. Johs, J.A. Woollam, InP optical constants between 0.75 and 5.0 eV determined by variable-angle spectroscopic ellipsometry, J. Appl. Phys. 77 (1995) 1715–1724. https://doi.org/10.1063/1.358864.

[72] D.E. Aspnes, The Accurate Determination of Optical Properties by Ellipsometry, in: Handb. Opt. Constants Solids, Elsevier, 1997: pp. 89–112. https://doi.org/10.1016/b978-012544415-6.50008-x.

Vita

Mohan Raj Rajkumar was born in Bangalore, India. He received his Bachelor of Engineering in Mechanical Engineering from Sir M. Visvesvaraya Institute of Technology in May of 2018. Following which he came to University of Texas at El Paso (UTEP) for his graduate studies as a Master of Science student in Mechanical Engineering.

Contact Information: <mohanraj7rajkumar@gmail.com>